GEOLOGICA CARPATHICA, OCTOBER 2018, 69, 5, 439–452 doi: 10.1515/geoca-2018-0025

Hydrothermal-to-metasomatic overprint of the neovolcanic rocks evidenced by composite apatite crystals: a case study from the Maglovec Hill, Slanské vrchy Mountains, Slovakia

NOEMI MÉSZÁROSOVÁ[1,2,✉], ROMAN SKÁLA[1,2], ŠÁRKA MATOUŠKOVÁ[1], PETR MIKYSEK[1,3], JAKUB PLÁŠIL[4] and IVANA CÍSAŘOVÁ[5]

[1]Institute of Geology of the Czech Academy of Sciences, Rozvojová 269, 165 00 Praha 6, Czech Republic; ✉meszarosova@gli.cas.cz
[2]Institute of Geochemistry, Mineralogy and Mineral Resources, Faculty of Science, Charles University, Albertov 6, 128 43 Praha 2, Czech Republic
[3]Institute of Geological Sciences, Faculty of Science, Masaryk University, Kotlářská 2, 611 37 Brno, Czech Republic
[4]Institute of Physics of the Czech Academy of Sciences, Na Slovance 2, 182 21 Praha 8, Czech Republic
[5]Department of Inorganic Chemistry, Faculty of Science, Charles University, Hlavova 6, 128 43 Praha 2, Czech Republic

(Manuscript received November 1, 2017; accepted in revised form October 4, 2018)

Abstract: The apatite assemblage from Maglovec hill (Slanské vrchy Mountains near the city of Prešov) from fissures of hydrothermally altered neovolcanic rocks (andesites and related lithologies) was studied. The assemblage consists of two different morphological apatite types (apatite in cores of prismatic crystals and fibrous apatite mantling these cores). The assemblage was investigated by a multi-analytical approach to reveal its unique chemical composition and structure. Both types of apatite display zoning visible in back-scattered electron (BSE) images. Core apatite is relatively homogenous with porous rims appearing darker in the BSE images at the contact with fibrous apatite, and occasionally with darker regions along fractures. These parts are depleted in trace elements, mostly in LREE. Fibrous apatites display concentric and/or patchy zoning. Dark regions in fibrous apatite occasionally display a porous structure. In part of fibrous crystals, substitution of $(CO_3)^{2-}$ for phosphorus is confirmed by Raman spectroscopy by the presence of a band at ~1071 cm^{-1}. This method also confirmed the presence of OH in different populations in the structure of all apatite types. The three most important observed peaks are caused by vibrations of hydroxyls influenced by different adjacent anions: hydroxyl (band at ~3575 cm^{-1}); fluorine (band at ~3535–3540 cm^{-1}); chlorine (band at ~3494 cm^{-1}). In REE-depleted parts of both apatite types, fine inclusions of monazite and rarely Th-rich silicate are observed. The acquired data suggest a hydrothermal origin of this assemblage and indicate a formation sequence of distinct apatite types. Moreover, minerals from the epidote group were identified, which have not been described from this locality before as well as vanadium-rich magnetites that form exsolution lamellae in ilmenite grains.

Keywords: hydrothermal alteration, crystal chemistry, apatite, REE, SCXRD, PXRD, EPMA, SEM, LA–ICP–MS, Raman spectroscopy.

Introduction

An apatite assemblage occurring on the southern slopes of Maglovec hill near the city of Prešov is unique due to its unusual chemical composition caused by multiple dissolution and recrystallization metasomatic events. No other similar locality with such a complex apatite assemblage has been known to date.

Apatite group minerals (expressed by the general formula as $Ca_5(PO_4)_3X$ where X=F, Cl, OH) are a major object of study due to their variable composition at the locality. In general, the symmetry of minerals of the apatite group (further referred to as apatite) is consistent with the space group $P6_3/m$; however, ordering of ions in the structure may result in departures from an ideal structure reducing the symmetry to the monoclinic space group $P2_1/b$. Hydroxylapatite-*M* and chlorapatite-*M* represent such monoclinic apatite group minerals (Pasero et al. 2010). A large amount of chemical substitutions may take place for calcium and phosphorus but also for anions at position X of the apatite structure (Pan & Fleet 2002). Possibly the best investigated is the Ca, REE substitution, as it may generate intense luminescence (Gaft et al. 2001; Waychunas 2002; MacRae & Wilson 2008; Lenz et al. 2015). Another important substituent is the $(CO_3)^{2-}$ group which may substitute for either phosphorus in tetrahedra or anions at position X (Penel et al. 1998; Antonakos et al. 2007; Awonusi et al. 2007).

The uniqueness of this locality has been noticed before and, among others, it was subject to a detailed mineralogical study by Povondra et al. (2007). Their investigation revealed three types of apatite with very complex chemical compositions and suggested that Cl-rich varieties were monoclinic. The presence of extremely fine fibrous carbonate–hydroxylapatite was also pointed out. In the mineral association of the apatite assemblage, opal located at the centers of prismatic apatite crystals and tremolite-asbestos were reported. The study, however, left some questions opened, in particular the apatite crystal structure and chemistry. The goal of this study is to expand knowledge on the chemical and structural data on minerals of this assemblage, and specifically to test the presence of monoclinic

apatite and explain the origin of such a complex apatite assemblage. Therefore, multi-analytical approach and detailed textural study were used: scanning electron microscopy, electron probe microanalysis, laser ablation inductively coupled plasma mass spectrometry, Raman spectroscopy, and powder and single-crystal X-ray diffraction. Characteristics of previously reported phases is supplemented by chemical characteristics of several new minerals for the locality.

Locality description

Maglovec Hill is located in the northern part of the Slanské vrchy Mountains 8 km ENE of the city of Prešov near the village of Vyšná Šebastová (Fig. 1; 49°01'13" N, 21°20'31" E). Local rock was characterized by Kuthan (1948) as porphyric augite andesite. In some parts of the rock, pyroxenes are transformed to amphiboles and the rock can be described as porphyric amphibole andesite. Marcinčáková & Košuth (2011) classified the rock as diorite porphyrite formed by over 50 % plagioclase microlites. The diorite porphyrite contains xenoliths including rock types ranging from volcaniclastics to sediments or xenoliths with Ca-skarn mineralization.

The studied mineral assemblage forms fracture fillings in tectonic zones of hydrothermally altered host rock (Černý et al. 1973; Povondra et al. 2007). The mineral association from magmatic to supergene stage was described in detail by Ďuďa et al. (1981). According to these authors, the apatite mineral assemblage includes two types of apatite (one produced during post-magmatic stage while the other originated during a supergene stage), calcic amphibole displaying higher than stoichiometric content of water, chabazite, ilmenite, calcite, hematite, kaolinite, limonite and a mixture of Ti-oxides.

Analytical methods

The apatite assemblage and its host rock were characterized in three polished sections prepared as grain mounts from 14 samples. All samples were taken from the material studied by Povondra et al. (2007).

Seven samples include apatite assemblage; three of them were oriented cuts (Fig. 2; either parallel or perpendicular to *c* axis) and others represented general cuts (though one of them was almost perpendicular to *c* axis). Five samples included asbestos associated with solitary small grains of apatite and with surrounding host rock. Two samples represented the host rock.

Zoning of all minerals was investigated by a scanning electron microscope (SEM). Back-scattered electron (BSE) images and element distribution maps were obtained by a Tescan Vega 3XMU scanning electron microscope equipped with a Bruker X'Flash 5010 energy dispersive X-ray spectrometer housed at the Department of Analytical Methods, Czech Academy of Sciences, Institute of Geology, Prague.

Major element composition

Major element concentrations were obtained by a CAMECA SX-100 electron probe microanalyzer (EPMA) equipped with four wavelength-dispersive X-ray spectrometers, housed at the Department of Analytical Methods, Czech Academy of Sciences, Institute of Geology, Prague. For analyses of apatites, the accelerating voltage of 15 kV, the sample current of 10 nA, and an electron beam of 2 μm diameter were applied; focused beam was used for the measurement of grains too small to use the 2 μm beam spot. In such grains, the same voltage and current were applied as for defocused beam. The analyzed elements included (used spectral line, spectrometer crystal, standard, average detection limit in ppm, respectively, are given in parentheses): F (*Kα*, PC0, fluorite, 1322), Na (*Kα*, TAP, jadeite, 782), Mg (*Kα*, TAP, periclase, 295), Al (*Kα*, TAP, jadeite, 352), Si (*Kα*, TAP, quartz, 358), P (*Kα*, LPET, apatite, 553), S (*Kα*, LPET, barite, 110), Cl (*Kα*, LPET, tugtupite, 362), Ca (*Kα*, LPET, apatite, 535), Fe (*Kα*, LLIF, hematite, 710), Sr (*Lα*, LPET, celestite, 338), Y (*Lα*, LPET, Y-Al garnet, 369), La (*Lα*, LLIF, monazite, 954), Ce (*Lα*, LLIF, monazite, 1155), Pr (*Lβ*, LLIF, REE glass, 2335), Nd (*Lα*, LLIF, monazite, 1044). Analyses of apatites were recalculated based on 13 anions (O^{2-}, F^- and OH^-) per formula unit. The content of H_2O was calculated from stoichiometry assuming full occupancy of X site. Analytical conditions and procedures taken to calculate empirical formulae of other minerals are listed in the electronic supplement.

Trace element composition

Trace element concentrations were determined using laser ablation inductively coupled plasma mass spectrometry (LA–ICP–MS) housed at the Department of Geological Processes, Czech Academy of Sciences, Institute of Geology, Prague. The operating conditions of the sector field ICP–MS (Thermo-Finnigan Element 2) were optimized using a multi-element tuning solution to comply with a high sensitivity accompanied by the oxide ion percentage of less than 0.5 %. Isotopes were measured either in low mass resolution (m/Δm=300) or in medium resolution (m/Δm=4000). The isotopes measured in low mass resolution included: ^{7}Li, ^{9}Be, ^{11}B, ^{23}Na, ^{43}Ca, ^{75}As, ^{85}Rb, ^{89}Y, ^{90}Zr, ^{93}Nb, ^{121}Sb, ^{133}Cs,

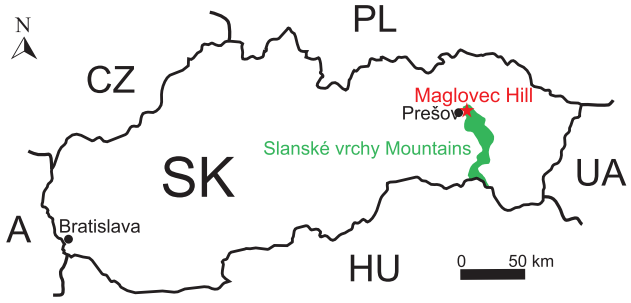

Fig. 1. A location map of Maglovec Hill marked with an asterisk.

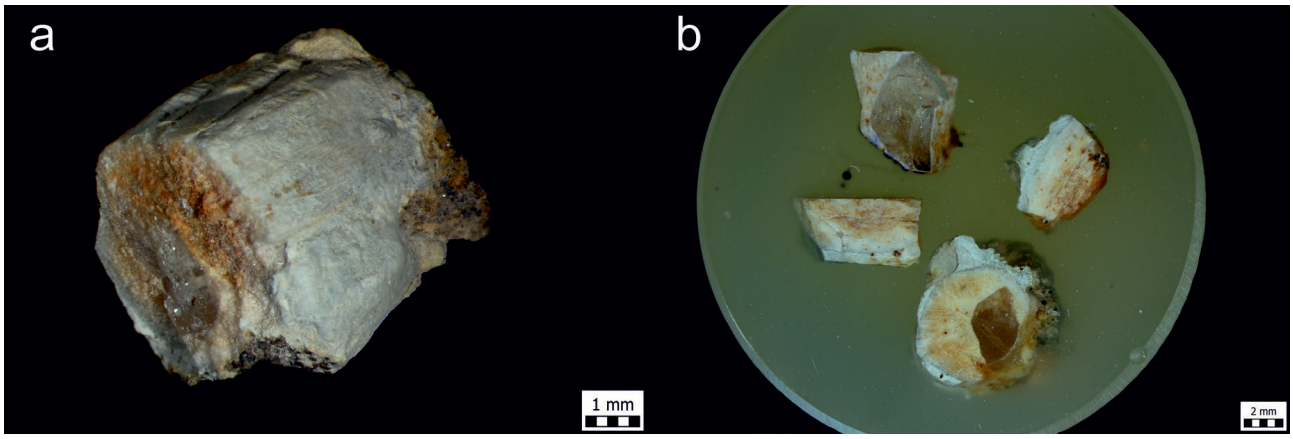

Fig. 2. Appearance of apatite assemblage. **a** — A macrograph of a prismatic crystal of apatite which is composed of clear yellowish inner part of core apatite and rusty-orange to white fibrous apatites mantling the core apatite. **b** — A photograph of a polished section of oriented cuts of apatite assemblage illustrating the relationship of two apatite types.

^{139}La, ^{140}Ce, ^{141}Pr, ^{146}Nd, ^{147}Sm, ^{153}Eu, ^{157}Gd, ^{159}Tb, ^{163}Dy, ^{165}Ho, ^{166}Er, ^{169}Tm, ^{172}Yb, ^{175}Lu, ^{178}Hf, ^{181}Ta, ^{182}W, ^{185}Re, ^{208}Pb, ^{209}Bi, ^{232}Th, ^{238}U. The isotopes measured in medium mass resolution included: ^{23}Na, ^{24}Mg, ^{27}Al, ^{29}Si, ^{31}P, ^{32}S, ^{43}Ca, ^{45}Sc, ^{47}Ti, ^{51}V, ^{52}Cr, ^{55}Mn, ^{59}Co, ^{60}Ni, ^{63}Cu, ^{66}Zn, ^{209}Bi.

A laser with beam diameter of 30 μm was rastered over lines 50 μm long. Two lines for both resolutions were measured in each grain, if the apatite grain size allowed. All concentrations were calibrated against the external standard reference materials — synthetic silicate glass NIST SRM 612 (Jochum 2011) and synthetic phosphate glass STDP3-150 (Klemme et al. 2008). The isotope of ^{43}Ca was used as an internal standard for both resolutions using chemical data (CaO content) obtained previously by EPMA. The time-resolved signal data were processed using the Glitter software (van Achterbergh et al. 2001) to select signal parts free of any other mineral/fluid inclusions and inhomogeneities. Following elements were below their detection limits or the results of measurements were unreliable due to analytical artefacts; consequently they are not included in results: Be, Na, Mg, Sc, Ti, Cr, Fe, Co, Ni, Cu, Zn, As, Ta, W, Re, Bi.

Raman spectroscopy

Raman spectra were obtained with an S&I MonoVista CRS+ Raman microspectrometer (spectrometer SP2750i, Princeton Instruments) equipped with a Peltier-cooled iDus-416 detector (Andor, size 2000×256 pixels, pixel size 15×15μm) housed at the Department of Analytical Methods, Czech Academy of Sciences, Institute of Geology, Prague. The accuracy of the wavenumber axis was calibrated with Hg–Ne–Ar lamp (by Princeton Instruments) and before every set of measurements spectra of standards (polystyrene and silicon or quartz) were obtained as a reference. In all measurements, a laser beam was focused on a sample surface with a 50× magnifying long working distance objective attached to an Olympus BX-51WI microscope. Excitation lasers of 3 different wavelengths (488 nm, 532 nm, 785 nm) were used to document laser-induced photoluminescence (PL). Spectra documenting PL were obtained with 150 grooves/mm grating resulting in ~100–7000 cm^{-1} range with 488 nm excitation, in ~100–6300 cm^{-1} range with 532 nm excitation, and ~100–3500 cm^{-1} range with 785 nm excitation. Spectra were collected for 5 sec in 10 consecutive accumulations (488 nm excitation) or for 10 sec in 10 consecutive accumulations (532 nm excitation and 785 nm excitation). For detailed study of vibration modes of apatite structure including determination of the presence of $(CO_3)^{2-}$, the Raman spectra were acquired within ~120–1150 cm^{-1} range with 488 nm excitation laser to eliminate the most interfering PL signal. Spectra were collected for 30 sec in 10 consecutive accumulations. For a detailed study of vibration modes of populations of hydroxyl group, the Raman spectra were collected within 3300–3700 cm^{-1} range using the same condition of accumulations but with a 532 nm excitation laser which minimized the influence of PL signals in this spectral region. Spectra for identification of host rock minerals were recorded within ~100–1250 cm^{-1} except for those containing H_2O in their structure; in the case of H_2O/OH-bearing minerals, spectra were collected up to 4000 cm^{-1}. Spectra were recorded with 488 nm excitation laser for 10 sec in 2 consecutive accumulations with exception of spectra of ilmenite and magnetite which were obtained with 785 nm excitation laser for 30 sec in 5 consecutive accumulations. All Raman spectra were background-corrected and spectral bands were fitted by pseudo-Voigt function in the Fityk 0.9.8. program (Wojdyr 2010).

Powder X-ray diffraction

X-ray powder diffraction investigation was carried out with a Bruker D8 Discover diffractometer (housed at the Department of Analytical Methods, Czech Academy of Sciences, Institute of Geology, Prague) equipped with a silicon-strip linear LynxEye detector and a focusing germanium primary

monochromator of Johansson type providing Cu$K\alpha_1$ radiation (λ=1.54056 Å). Data for mineral identification were collected in the 2θ range of 3–70° with a step size of 0.014° and a counting time of 2.5 seconds at each step, and detector angular opening of 1.507°. Data for apatite structure characterization were collected in the 2θ range of 8–140° with a step size of 0.009° and a counting time of 3.5 second at each step, and detector angular opening of 2.896°. Data for actinolite-asbestos structure characterization were collected in the 2θ range of 4–140° with a step size of 0.009° and a counting time of 3.5 second at each step, and detector angular opening of 1.996°. The phase identification was performed with DIFFRAC.EVA software (Bruker AXS GmbH, Karlsruhe, Germany, 2016). The structure refinements of both apatites and actinolite-asbestos were performed with DIFFRAC.TOPAS software (Bruker AXS GmbH, Karlsruhe, Germany, 2008) using crystal structures from Hughes et al. (1989) as starting models for apatites. For actinolite-asbestos, the fitting was carried in monoclinic *C*2/*m* space group using the model for actinolite provided by DIFFRAC.TOPAS software distribution.

Single-crystal X-ray diffraction

Crystal structures of four crystals were refined from single-crystal X-ray diffraction data. Two of the crystals corresponded to apatite cores, the other two were sampled from fibrous sheath of the larger prismatic crystals. Data for two crystals were collected using an Oxford Diffraction Gemini single-crystal diffractometer system, equipped with an Atlas CCD area detector, using monochromatized Mo*K*α radiation, λ=0.71073 Å, and with a fibre-optics Mo-Enhance collimator (housed at the Czech Academy of Sciences, Institute of Physics, Prague). Other two crystals were characterized with a Nonius Kappa CCD diffractometer, using monochromatized Mo*K*α radiation (Department of Inorganic Chemistry, Faculty of Science, Charles University, Prague). The final crystal structure refinement was carried out by the Jana2006 program (Petříček et al. 2014) with atomic coordinates taken from Hughes et al. (1989) as a starting model.

Results

Apatite assemblage

Two morphologically different types of apatite can be distinguished; (i) a clear yellowish apatite forming cores of prismatic crystals, herein called core apatite, and (ii) reddish rusty-orange to white fibrous apatite mantling the cores, herein called fibrous apatite (Fig. 2). The core apatites and the fibrous apatites share roughly the same crystallographic orientation; the only exception are the finest fibrous apatites which tend to be randomly oriented at some places. No opal was observed in the centres of core apatite in the set of studied samples, in variance with Povondra et al. (2007). This apatite assemblage is surrounded by white to greyish light green extremely fine-fibrous asbestos.

Fragments of **core apatite** reach up to 4 mm in diameter and 6 mm in length. Core apatite is relatively homogenous with darker rims in the BSE images at the contact with fibrous apatites (Fig. 3). Homogenous parts of core apatite are further referred to as ApCore. The rims, further referred to as ApRim, appear porous and they gradually transit into fibrous apatites. In regions where the crystals of ApCore are fractured and filled with asbestos, zones darker in the BSE images occasionally appear along these fractures (Fig. 3). Rarely, some inclusions of monazite occur (Fig. 3).

Contents of fluorine and partly also chlorine in apatites are strongly influenced by diffusion to the surface from depth below the analysed region due to electrical field produced by the electron beam (Stormer et al. 1993; Goldoff et al. 2012; Stock et al. 2015). This phenomenon is a function of many variables; orientation of analyzed apatite crystals being one of them. Due to this phenomenon the most reliable values of fluorine and chlorine contents were obtained from the samples with no specific crystallographic orientation; therefore only analytical data of non-oriented grains for both types of core apatite are presented in Table 1. Some substitution for calcium and phosphorus were determined from major element composition of ApCore. The position normally fully occupied by Ca is partly substituted by REEs (almost 2 wt. %) and also by low contents of Na, Fe and Mg. Tetrahedral structural position normally fully occupied by phosphorus shows a weak Si substitution. ApCore shows the highest contents of REE and particularly LREE (notably La, Ce, Pr and Nd). Trace element concentrations including REE contents in ApCore are given in Supplementary Table S1.

Raman spectroscopy investigation applied to ApCore samples revealed well defined vibration bands assigned to apatite structure. Table 2 summarizes values of Raman shifts for all peaks of representative samples of each chemical type. Corresponding Raman spectra are displayed in Figure 4. The most intensive peak of ν_1 vibration of tetrahedron $(PO_4)^{3-}$ is at 962.6 cm^{-1}; in the area of ν_2 vibration modes of $(PO_4)^{3-}$, two peaks are observed at 429.8 and 448.1 cm^{-1}. In the region of ν_3 vibration modes of $(PO_4)^{3-}$, six peaks can be resolved at 1041.0 cm^{-1}, 1048.2 cm^{-1}, 1054.2 cm^{-1}, 1059.9 cm^{-1}, 1078.1 cm^{-1} and 1087.6 cm^{-1}. In the region of ν_4 vibration modes of $(PO_4)^{3-}$, three peaks are observed at 581.8 cm^{-1}, 590.6 cm^{-1} and 608.0 cm^{-1}. Presence of OH was confirmed by Raman spectroscopy. In the region of stretching vibration modes of OH group at ~3500 cm^{-1}, four peaks are resolved at 3442.6 cm^{-1}, 3470.7 cm^{-1}, 3497.9 cm^{-1} and 3535.8 cm^{-1}. Peaks in the Raman spectra of ApRim are slightly shifted in comparison to ApCore due to different chemical composition of the two types (Table 2.). The most notable shifts to lower wavenumbers are observed in the region of ν_3 vibration modes of $(PO_4)^{3-}$. In the region of the vibration modes of hydroxyl, four peaks are also resolved but only two of them coincide with those observed in spectra of ApCore (at 3494.0 cm^{-1} and 3540.1 cm^{-1}). This observation reflects the different occupation of X position.

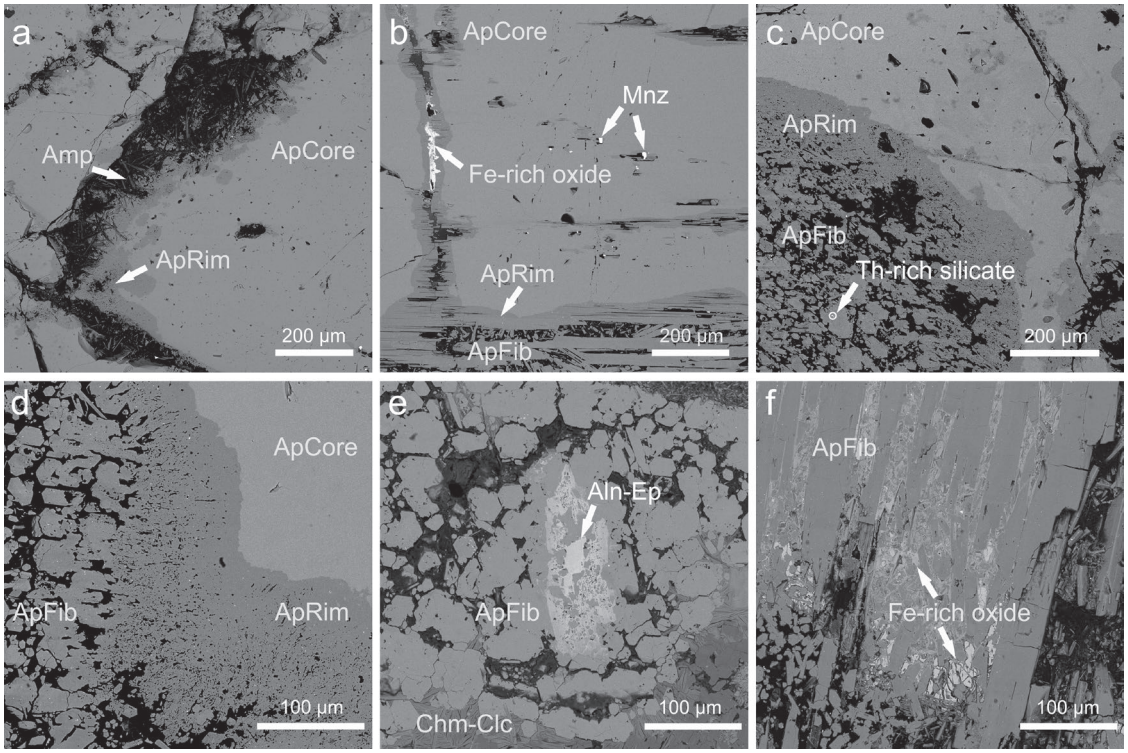

Fig. 3. BSE images of an apatite crystal forming the core of the apatite assemblage which is embayed in fibrous apatite crystals. **a** — Darker regions in BSE (ApRim) along cracks filled with very fine actinolite-asbestos. **b** — Core apatite (ApCore) with fractures healed with Fe-rich oxides including some monazite inclusions with the rim transition into fibrous apatites. **c** — Core apatite displaying mottled structure with darker regions rimmed with dark parts passing to fibrous apatite; both apatite types are roughly oriented perpendicular to the *c* axis. A thorium-rich silicate inclusion in fibrous apatite is marked with an arrow. **d** — A homogeneous part of ApCore rimmed with a darker region with porous structure (ApRim) passing to fibrous apatite with mottled structure. **e** — An assemblage of fibrous apatites replaced by epidote-group minerals in contact with chlorites. **f** — Apatite fibers of variable size coated with Fe-rich oxides. Abbreviations: Amp — amphibole, ApCore — core apatite bright in the BSE images; ApRim — core apatite dark in the BSE images; ApFib — fibrous apatite, Aln–Ep — epidote-group minerals, Mnz — monazite.

Moreover, very intense peaks which cannot be assigned to vibrations of apatite structure were obtained in the spectra of all samples. In some cases, these peaks partly overlap the Raman spectra of apatite. Three different excitation lasers were used to record spectra of all chemical types of apatites to find out the origin of these peaks. After converting the Raman shifts to wavelength, it appeared that some of the peaks occur at the same wavelength values. This fact suggests that these peaks correspond to laser induced photoluminescence (PL). To illustrate this feature, the spectra of ApCore for which the highest intensity of these peaks were observed among all studied samples are shown in Figure 5.

Both the single-crystal and powder X-ray diffraction studies of the core apatites unambiguously revealed the hexagonal symmetry for this material. Crystal structure parameters refined from single-crystal X-ray diffraction data are listed in Supplementary Table S2; results of refinement of powder X-ray diffraction data are listed in Table 3.

Fibrous apatite

The size of fibrous crystals varies significantly; the largest crystals are as long as 500 µm and up to 70 µm wide, whereas the smallest crystals rarely exceed 50 µm in length and are not wider than 5 µm. In the BSE images, most grains display concentric and/or patchy zoning. This structure is caused by the differences in the composition of individual regions, particularly differences in the contents of F and Cl as shown on elemental distribution maps (Fig. 6). A total of 56 points were measured in larger grains and 28 points in smaller grains. Five distinct chemical types can be resolved among fibrous apatites (Table 1). The BSE images allow us to distinguish three different groups of fibrous apatite: 1) BSE-dark grains with porous structure, referred to as ApFib1, 2) BSE-dark grains without porous structure, referred to as ApFib2, and 3) BSE-bright grains. Based on the occupancy of the X site, the group of fibrous apatites bright in the BSE images is further divided into two chemically distinct types: ApFib3 and ApFib4 (Fig. 7). ApFib3 contains slightly elevated content of fluorine whereas ApFib4 lacks fluorine almost completely. The size of the finest apatite fibres prevented the observation of any zoning, however, their chemical composition in general overlaps that of the larger grains; nevertheless, some grains differ constituting a separate chemical group, referred to as ApFib5. In all types of fibrous apatite, only minor substitutions of silicon for phosphorus and REE for calcium was observed.

Table 1: Average chemical composition of two types of core apatite and different chemical types of fibrous apatite.

	ApCore		ApRim		ApFib1		ApFib2		ApFib3		ApFib4		ApFib5	
	n=15	σ	n=6	σ	n=8	σ	n=14	σ	n=9	σ	n=12	σ	n=9	σ
P_2O_5	42.2	0.32	43.02	0.35	42.84	0.50	42.48	0.76	41.96	0.36	41.13	0.47	40.84	0.92
SiO_2	0.40	0.06	0.04	0.04	0.12	0.05	0.26	0.08	0.23	0.08	0.63	0.06	0.60	0.03
Y_2O_3	0.17	0.03	0.09	0.03	0.09	0.06	0.13	0.06	0.09	0.04	0.18	0.04	0.21	0.02
La_2O_3	0.47	0.06	b.d.l.	b.d.l.	b.d.l.	b.d.l.	b.d.l.	b.d.l.	b.d.l.	b.d.l.	0.01	0.06	0.06	0.06
Ce_2O_3	1.12	0.12	b.d.l.	b.d.l.	0.04	0.08	0.15	0.13	0.22	0.04	0.48	0.08	0.51	0.07
Nd_2O_3	0.37	0.07	b.d.l.	b.d.l.	0.03	0.05	0.11	0.01	0.07	0.06	0.26	0.06	0.30	0.05
FeO	0.36	0.04	b.d.l.	b.d.l.	b.d.l.	b.d.l.	b.d.l.	b.d.l.	b.d.l.	b.d.l.	b.d.l.	b.d.l.	0.02	0.06
MgO	0.14	0.02	b.d.l.	b.d.l.	b.d.l.	b.d.l.	b.d.l.	b.d.l.	b.d.l.	b.d.l.	b.d.l.	b.d.l.	b.d.l.	b.d.l.
CaO	53.11	0.58	56.53	0.87	56.39	0.72	55.69	0.75	55.3	0.84	54.87	0.89	56.37	0.91
SrO	0.07	0.02	b.d.l.	b.d.l.	b.d.l.	b.d.l.	0.00	0.01	0.03	0.03	0.02	0.02	0.01	0.01
Na_2O	0.30	0.05	b.d.l.	b.d.l.	b.d.l.	b.d.l.	0.001	0.02	b.d.l.	b.d.l.	b.d.l.	b.d.l.	b.d.l.	b.d.l.
F	2.72	0.18	3.10	0.34	2.58	0.66	2.29	0.49	1.13	0.34	0.22	0.07	0.70	0.10
Cl	1.65	0.24	0.84	0.12	1.05	0.53	0.95	0.47	3.02	0.24	3.11	0.18	2.46	0.13
H_2O (calc)	0.08	0.05	0.15	0.15	0.33	0.25	0.48	0.16	0.48	0.10	0.88	0.05	0.83	0.06
O=F, Cl	1.52	n.d.	1.50	n.d.	1.33	n.d.	1.17	n.d.	1.16	n.d.	0.79	n.d.	0.84	n.d.
Total	101.65	0.92	102.26	1.12	102.14	1.14	101.37	1.16	101.37	1.02	101.07	1.16	102.05	1.01
P	2.995	0.013	2.999	0.019	2.993	0.012	2.989	0.023	2.984	0.015	2.946	0.016	2.905	0.036
Si	0.035	0.006	0.003	0.004	0.01	0.005	0.023	0.007	0.02	0.007	0.056	0.005	0.053	0.003
Y	0.008	0.002	0.004	0.001	0.004	0.003	0.006	0.003	0.004	0.002	0.008	0.002	0.01	0.001
La	0.014	0.002	0.000	0.000	0.000	0.000	0.000	0.000	0.000	0.000	0.003	0.002	0.002	0.002
Ce	0.035	0.003	0.000	0.000	0.001	0.002	0.005	0.004	0.007	0.001	0.015	0.002	0.016	0.002
Nd	0.011	0.002	0.000	0.000	0.001	0.001	0.003	0.003	0.002	0.002	0.008	0.002	0.009	0.002
Fe	0.025	0.003	0.000	0.000	0.000	0.000	0.000	0.000	0.000	0.000	0.000	0.000	0.002	0.004
Mg	0.018	0.003	0.000	0.000	0.000	0.000	0.000	0.000	0.000	0.000	0.000	0.000	0.000	0.000
Ca	4.770	0.030	4.988	0.044	4.987	0.027	4.961	0.056	4.978	0.042	4.973	0.039	5.075	0.087
Sr	0.003	0.001	0.000	0.000	0.000	0.000	0.000	0.001	0.001	0.001	0.001	0.001	0.000	0.001
Na	0.049	0.008	0.000	0.000	0.000	0.000	0.001	0.003	0.000	0.000	0.000	0.000	0.000	0.000
F	0.722	0.049	0.808	0.084	0.672	0.169	0.601	0.128	0.300	0.087	0.058	0.018	0.185	0.026
Cl	0.234	0.033	0.116	0.016	0.146	0.075	0.134	0.066	0.431	0.036	0.445	0.029	0.350	0.021
OH	0.044	0.027	0.081	0.082	0.182	0.142	0.266	0.088	0.269	0.057	0.497	0.023	0.465	0.029
M	4.933	0.031	4.992	0.044	4.993	0.026	4.975	0.055	4.992	0.041	5.007	0.038	5.113	0.085
T	3.030	0.012	3.002	0.018	3.004	0.010	3.012	0.021	3.004	0.017	3.001	0.015	2.958	0.034
Fap	0.722		0.808		0.672		0.601		0.300		0.058		0.185	
Clap	0.234		0.116		0.146		0.134		0.431		0.445		0.350	
OHap	0.044		0.081		0.182		0.266		0.269		0.497		0.465	

Explanatory notes: b.d.l. — below detection limits; σ — standart deviation; n — number of analyses used for calculation of average composition; n.d. — not determined because of low numbers of observation

The latter substitutions were observed in types ApFib3, ApFib4 and ApFib5. Trace element concentrations in fibrous apatites are listed in Supplementary Table S1. Collection of data from chemically diverse parts of crystals was prevented by the limited spatial resolution of the LA–ICP–MS technique. Consequently, many differences in element contents from the herein reported individual measurements can be attributed to the actual lateral position sampled by the laser beam. Analyses marked ApFib-26a* and ApFib-26b* were acquired in large zones significantly brighter in BSE, embayed in fibrous apatite and chemically closely resembling the ApCore type. Compared to the ApCore, fibrous apatites display a depletion in most trace elements (see Table S1). Raman spectra of chemically distinct types were recorded to document a possible shift due to different occupancy of X sites. For the ApFib1 and ApFib2 types, Raman vibration modes of apatite structure are invariant, and both types are presented as the ApFib1-2 type. Raman shifts are listed in Table 2 and Raman spectra are displayed in Figure 4. The Raman spectra of ApFib3 and ApFib4 are quite similar with some small shifts. Raman spectra of ApFib1–2 and ApFib5 differ from those of ApFib3 and ApFib4 and also mutually, mainly in the regions of ν_3 vibration modes of $(PO_4)^{3-}$ and the region of stretching vibration modes of OH group (see Fig. 4). To point out the most interesting observation suggesting the presence of $(CO_3)^{2-}$ substituted for phosphorus, a peak at 1070 cm^{-1} was resolved by fitting in spectra of ApFib3, ApFib4 and ApFib5 in the region of the ν_3 vibration modes of $(PO_4)^{3-}$.

Fibrous apatite mantling the core apatite was subjected to a detailed powder X-ray diffraction study. Several samples were tested pointing out that the material is a complex mixture quite often containing amphibole in addition to apatite phases. Finally, a single specimen was identified that was free of any contamination. Careful Rietveld fitting for a sample consisting

of fibrous apatite applying constrains on unit-cell dimension sizes provided a satisfactory fit for a mixture of five individual apatite-structured phases of hexagonal symmetry (Fig. 8, Table 3). No superstructure peaks due to anion ordering resulting in monoclinic $P2_1/b$ space group and doubling *b* axis was found. The character of the fibrous aggregate did not allow an association of individual chemical groups with particular structure data.

Table 2: Summary of Raman shifts for all vibration peaks for representative samples of each chemical type of apatites.

Sample	ApCore	ApRim	ApFib1-2	ApFib3	ApFib4	ApFib5
lattice				99.6		
	133.1	132.7	133.5	126.8	122.6	125.8
		138.4	138.6			
	152.7	154.0	156.1	143.5		141.9
		181.7	181.3			
	208.9	209.0	209.8	203.1	202.9	196.8
		232.3	233.0			229.7
				240.9	240.6	
		289.3	289.2		284.2	282.2
		306.2	307.0	302.3	306.0	301.4
ν_1	962.6	962.3	962.0	959.2	959.0	959.1
ν_2	429.8	429.7	429.5	428.1	428.1	428.0
	448.1	447.3	448.6	442.6	440.5	438.7
ν_3	1041.0			1019.4	1019.2	
	1048.2	1032.5	1030.9	1031.0	1031.9	1029.8
	1054.2	1042.7	1040.7	1039.0	1039.3	1039.9
	1059.9	1048.8	1049.2	1047.3	1047.6	
	1078.1	1056.5	1056.8	1060.2	1061.1	1052.2
	1087.6	1076.7	1077.4	1075.0	1075.0	1075.0
ν_1 CO_3				1070.0	1070.0	1070.0
ν_4	581.8	579.9		585.7	585.8	577.4
	590.6	590.6	590.5	590.5	590.6	590.6
	608.0	608.1	607.2	608.0	608.8	608.7
				619.8	618.9	618.4
REE-OH-F	3442.6				3451.5	3449.4
REE-OH-OH	3470.7			3468.7		
OH-Cl	3497.9	3494.0		3491.5	3495.7	3490.1
OH-F	3535.8	3540.1	3539.4	3539.1	3535.9	3535.0
OH-F-OH		3561.6	3560.6	3555.4	3553.8	
OH-OH		3579.0	3571.2	3573.3	3572.7	3575.0
Sr-OH			3582.2	3588.2	3587.9	
not assigned	3415.2	3399.2				3418.4
		3507.0	3506.3	3509.9	3512.3	

Host rock

The apatite assemblage comes from the fracture filling and hydrothermally altered part of the andesite body forming the Maglovec hill and it could be called tectonic fissure filling.

Minerals identified by the powder X-ray diffraction study of the bulk rock samples include chlorite, mica, amphibole supergroup minerals, plagioclase, apatite, titanite, ilmenite, epidote-group minerals, montmorillonite and kaolinite. The presence of the listed minerals apart from montmorillonite and kaolinite was confirmed by Raman spectroscopy. The Raman spectra of all minerals compared to matching standard spectra from the RRUFF database (Lafuente et al. 2015) are shown in the electronic supplement (Figs. S1–S10). The presence of ilmenite and magnetite was also confirmed by matching the measured spectral data to those reported by Wang et al. (2004). The specific chemical composition was reflected in the Raman spectra and some shifts consistent with the study by Wang et al. were observed (2004).

Besides apatite, the **major minerals** of the host rock include plagioclase, actinolite-asbestos and chlorite. **Plagioclase** forms xenomorphic grains in the matrix and also appears in the form of relicts of the original hypidiomorphic bladed or tabular crystals with a typical length of about 15 μm (Fig. 9). The matrix also contains radial spherical aggregates of thin sheets of **chlorite** (Fig. 9). These aggregates are typically 100 μm across with constituting sheets from 20 to 100 μm in length. Chlorites frequently occur associated with patchy-zoned micas and actinolite-asbestos. The variability observed in the BSE images illustrates chemical differences mostly in the contents of magnesium and iron. The chemical composition of chlorites based on the classification by Guggenheim et al. (2006) scatter around the middle of the solid solution between the chamosite and clinochlore end-members (Supplementary Fig. S11). The classification diagrams were taken from Zane & Weiss (1998) and from Plissart et al. (2009).

Actinolite-asbestos forms very fine fibres less than 1 μm wide and ranging from several microns to 30 μm in length. These fibres frequently form clusters. Long fibres are often curved and associated with relicts of original amphiboles or micas (Fig. 9). Occasionally they appear as inclusions in grains of epidote-group minerals (Fig. 9). They fill cracks in these grains and also spaces between the individual grains of other host rock minerals. In association with the apatite assemblage, they fill fissures in core apatite and also form clusters of fibres and rarely individual crystals found in spaces between fibrous apatites. The edges of the fibrous apatite assemblage are constantly in contact with actinolite-asbestos, gradually verging into it. The whole apatite assemblage is completely mantled by fibres and clusters of actinolite-asbestos. Frequently small (not more than 70 μm long and 50 μm wide) idiomorphic prismatic crystals of apatites are found in masses covering the fibrous apatites. The chemical composition of asbestos based on the classification by Hawthorne et al. (2012) corresponds to actinolite (Supplementary Fig. S12).

Minor minerals include micas, minerals of the epidote group, ilmenite and titanite. In some cases, aggregates of micas in association with titanite and ilmenite replace original minerals. Minerals of the **mica group** form platy crystals up to 200 μm long and 70 μm wide which display a significant patchy zoning in the BSE images (Fig. 9). Occasionally they

form clusters of very fine sheets displaying the zoning as well. The classification of micas was based on Rieder et al. (1998). The chemical composition of BSE-bright areas corresponds to annite while BSE-dark areas correspond to phlogopite (Supplementary Fig. S13). The classification diagram was taken from Tischendorf et al. (1997). **Ilmenite** forms hypidiomorphic grains, frequently replaced by titanite along the edges (Fig. 9). Size of ilmenite grains ranges from 20 to 300 µm across, and the grains are fractured in some cases. Magnetite exsolution lamellae appear in ilmenite grains occasionally; they are oriented parallel to each other suggesting their crystallographic orientation in host ilmenite grains. Rarely, inclusions of small (<10 µm in length) rounded prismatic crystals of apatite are associated with magnetite inclusions. **Titanite** frequently forms rims of ilmenite grains. Rarely, it is found as individual xenomorphic grains up to 20 µm in diameter occasionally associated with grains of epidote-group minerals or patchy-zoned micas. **Magnetite** exsolution lamellae in ilmenites have maximum lengths of 150 µm. The interior of these lamellae is occasionally fractured. The chemical composition of these magnetites is anomalous (see Supplementary Table S4). **Epidote-group minerals** form idiomorphic prismatic crystals or xenomorphic grains filling intergranular spaces. Both types of grain shapes display oscillatory, concentric, patchy zoning and/or combinations of both zonings in BSE images (Fig. 9). Crystals and grains are frequently fractured and contain a considerable amount of inclusions of other minerals (Fig. 9). In rare cases, replacements of fibrous apatite with minerals of the epidote group are found (Fig. 3). In BSE images, brighter and darker regions occur in crystals of both shape types; the bright zones frequently found in the centre of crystals correspond to allanite-(Ce) while the darker represent epidote (Supp. Fig. S14; Armbruster et al. 2006). Prismatic relicts of original **amphibole** are rare due to the decomposition into extremely fine fibrous actinolite-asbestos (Fig. 9). The size of these hypidiomorphic relicts ranges from 50 to 100 µm. Their chemical composition corresponds to edenite (Supp. Fig. S12). Occasionally, the cores of the relicts are darker in BSE images or display oscillatory zoning.

In one unique case, **Fe-rich oxides** are found as filling between crystals of individual apatite fibres (Fig. 3). These oxides partly replace original apatites; the process of replacement starts at grain boundaries. They are associated with several grains of iron-rich sulphide.

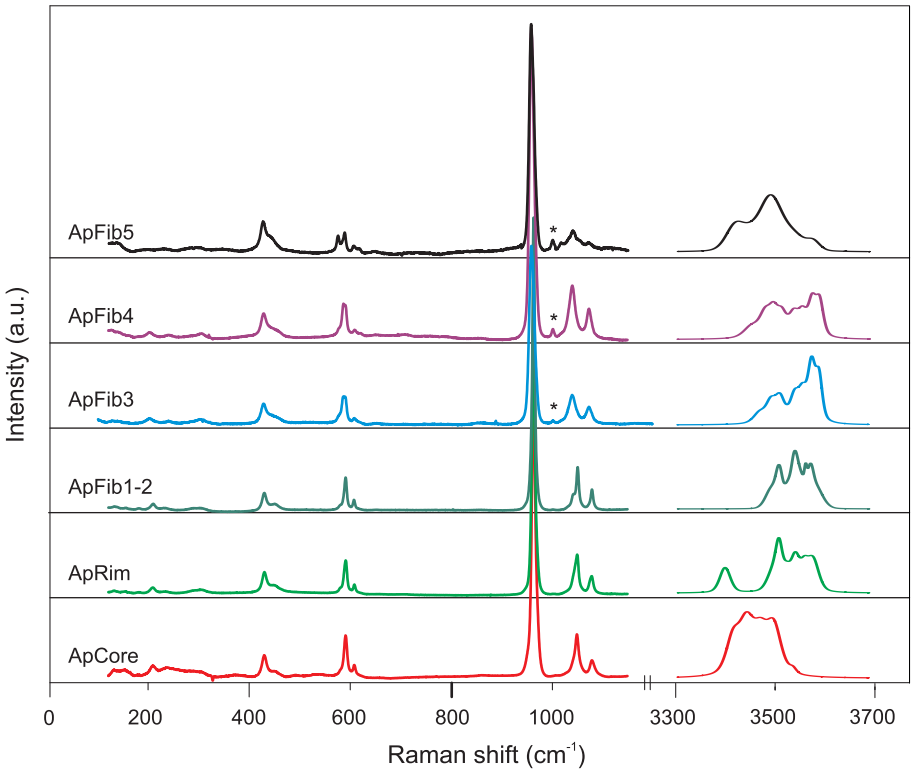

Fig. 4. Raman spectra of individual apatite types recorded in the range of ~100–1200 cm^{-1} and in the range of OH vibration modes ~3300–3700 cm^{-1}. The intensity scale for the range covering OH vibration modes is exaggerated. The peak marked with an asterisk is the most intense Raman peak of a resin used for sample adjustment.

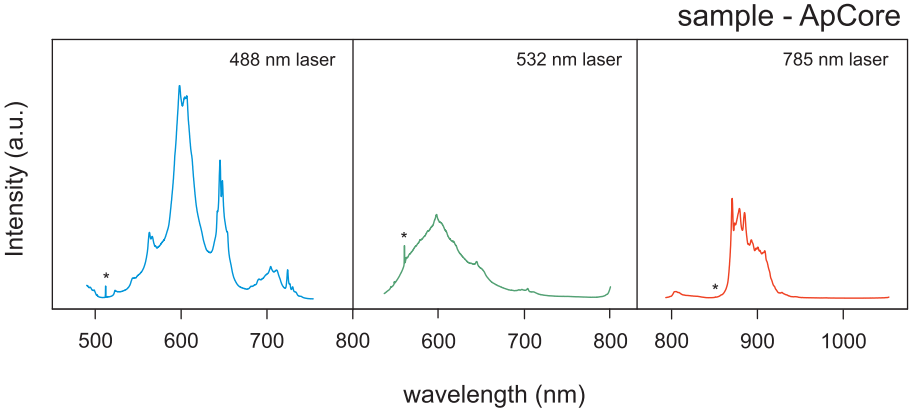

Fig. 5. Raman spectra of ApCore displaying laser-induced photoluminescence (PL) by three different excitation lasers. The most intense Raman vibration peak ν_1 $(PO_4)^{3-}$ is marked with an asterisk.

Table 3: Results of Rietveld fitting of data obtained by powder X-ray diffraction of core apatite and a mixture of fibrous apatites containing five individual apatite-structured phases.

	ApCore	ApFib-a	ApFib-b	ApFib-c	ApFib-d	ApFib-e
***a* (Å)**	9.4632(2)	9.5326(3)	9.4355(4)	9.5077(4)	9.4024(3)	9.4799(4)
***c* (Å)**	6.85623(17)	6.8419(3)	6.8669(9)	6.8532(12)	6.8821(4)	6.8599(4)
***V* (Å^3)**	531.73(3)	538.43(4)	529.44(8)	536.51(10)	526.90(5)	533.89(5)
c/a	1.380	1.393	1.374	1.387	1.366	1.382
content	100	37.5(9)	14.8(12)	25.1(11)	15.1(5)	7.5(5)
R_{exp} **(%)**	4.44, 5.08	3.07, 5.61				
R_{wp} **(%)**	8.37, 9.58	6.29, 11.5				
R_p **(%)**	5.81, 6.80	4.61, 9.39				
GOF	1.88	2.05				
DW	0.66	0.53				
R_{Bragg} **(%)**	4.178	2.521	1.632	1.049	2.039	3.015

Zircons and monazites (up to 50 μm in size) represent **accessory minerals**. Also, very small inclusions (maximum size 1 μm) of Th-rich silicate detected by EDS were found in fibrous apatites (Fig. 3). The chemical composition of the host rock minerals is given in Tables S3 and S4 in electronic supplement.

Discussion

Photoluminescence and Raman spectroscopy study

According to published data PL peaks can be attributed to the presence of Nd^{3+} and Sm^{3+} (Gaft et al. 2001; Waychunas 2002; MacRae & Wilson 2008; Lenz et al. 2015). Other peaks, however, may reflect the presence of other REEs but complete identification is prevented by massive overlaps. The assignment of these peaks to REEs corresponds well to the measured contents of trace elements (Supp. Table S1).

The positions of Raman bands vary depending on the occupancy of X site as well as the presence of $(CO_3)^{2-}$ at the tetrahedral site.

All the peak positions assigned to vibration of apatite structure of the distinct apatite composition types match published data (Table 2; Fig. 4). The most intensive vibration of apatite structure in the range 959–965 cm^{-1} corresponds to the ν_1 vibration of tetrahedron $(PO_4)^{3-}$. The position of vibration ν_1 of $(PO_4)^{3-}$ in fluorine-rich samples (ApCore, ApRim and ApFib1-2) is at higher wavenumbers of ~962 cm^{-1} while in chlorine and hydroxyl-enriched samples, it is shifted to ~959 cm^{-1}; the amount of this shift is proportional to the hydroxyl and chlorine contents at the X anion site (Penel et al. 1997; O'Donnell et al. 2009). In a similar way, the band position is influenced by the degree of $(CO_3)^{2-}$ substitution for phosphorus (Awonusi et al. 2007). In the range of ~428–450 cm^{-1}, ν_2 vibration modes of $(PO_4)^{3-}$ are observed in all samples. Shifts from ~450 cm^{-1} to lower wavenumbers of ~440 cm^{-1} are observable in chlorine-enriched samples ApFib3, ApFib4 and ApFib5 with increasing chlorine content (Penel et al. 1997; O'Donnell et al. 2009). The most significant shifts of Raman bands influenced by variations in chemical composition at X site and also with increasing carbonate content are found in the range of ~1020–1080 cm^{-1} which corresponds to ν_3 vibration modes of $(PO_4)^{3-}$ (Penel et al. 1998; Awonusi et al. 2007; O´Donnell et al. 2009). The ν_3 vibration modes of $(PO_4)^{3-}$ are split due to the departure from ideal tetrahedron symmetry into five to nine Raman-active vibration modes. The lowest wavenumbers for ν_3 vibration modes of $(PO_4)^{3-}$ are observed in chlorapatites (1020–1076 cm^{-1}); vibration modes in hydroxylapatites are observed in the range of 1030–1076 cm^{-1}; and in fluorapatite, the vibration modes are shifted to higher wavenumbers in the range of 1035–1080 cm^{-1}. The peak at ~1071 cm^{-1} is observed in carbonated apatites and is assigned to the combination of the carbonate mode ν_1 at 1070 cm^{-1} with one of the peaks of ν_3 $(PO_4)^{3-}$ vibration mode (in the range of ~1076–1084 cm^{-1} depending on chemical substitution of position X). The positions of peaks belonging to ν_3 $(PO_4)^{3-}$ in chlorine- and hydroxyl-rich samples ApFib3, ApFib4 and ApFib5 are shifted to lower wavenumbers than for samples ApFib1–2, ApCore and ApRim which are rich in fluorine. The combined peak of ν_3 $(PO_4)^{3-}$ and ν_1 $(CO_3)^{2-}$ vibration modes is observed in the spectra of samples ApFib3, ApFib4 and ApFib5. It is possible to resolve two separate peaks; one at 1070 cm^{-1} and other at 1075 cm^{-1}. This observation clearly indicates the presence of $(CO_3)^{2-}$ substituting for $(PO_4)^{3-}$ in their structure. The ν_4 vibration modes of $(PO_4)^{3-}$ are characterized by four peaks in the range of 580–620 cm^{-1} in hydroxylapatites and chlorapatites. In the case of fluorapatites, only two peaks are observed (Penel et al. 1997). A gradual disappearance of the first and the last peak is observed in the studied fluorine-rich samples (ApCore, ApRim and ApFib1–2). In the region of the stretching mode of vibration of OH group at ~3500 cm^{-1}, several peaks are resolved by fitting (Table 2, Fig. 4). The peaks in the area are affected by photoluminescence and have very low intensities. However, it is still possible to assign them to the vibration of different populations of hydroxyls in the apatite structure (Tacker 2004). A peak caused by vibrations of hydroxyls influenced by an adjacent hydroxyl is found at 3575 cm^{-1} and is further referred to as OH–OH. A peak caused by vibrations of hydroxyls influenced by adjacent fluorine is shifted to lower wavenumbers of 3535–3540 cm^{-1} and is referred to as OH–F. A peak caused by vibrations of hydroxyls influenced by adjacent chlorine is shifted even lower to 3494 cm^{-1} and is referred to as OH–Cl. All three peaks involving hydroxyls are stretching vibration of the OH group neighbouring to Ca. If Ca is substituted by another element, the peak is shifted to different wavenumbers. The Raman peak located at 3550 cm^{-1} can be either attributed to F–OH–F interaction in a specimen with low F concentration or explained as an interaction of OH–OH with a site occupied by Mn substituting for Ca. Substitutions of REEs shift the peak positions to

lower wavenumbers, in the case of vibration of OH–F to 3434 cm^{-1} and in the case of OH–OH to 3468 cm^{-1}. Vibration at position 3591 cm^{-1} is assigned to OH–OH vibration interacting with Sr replacing Ca (Table 2). The vibration OH–OH is observed in all samples with the exception of sample ApCore. This largely corresponds to the calculated concentration of OH in this particular sample which is very low and indicates that OH is not a neighbour to any other OH. Vibrations OH–Cl and OH–F are observed in all samples with varying intensities which reflect the amount of chlorine and fluorine contained in the samples. In addition to the already described atomic and molecular interactions producing the Raman signals summarized above, there are additional Raman peaks at ~3400–3420 cm^{-1} and ~3500–3512 cm^{-1} which cannot be assigned to any vibration described in the literature. In summary, it should be noted that the observed peaks correspond well to the concentrations of F, Cl and OH in the measured samples (Tables 1 and 2, Fig. 4).

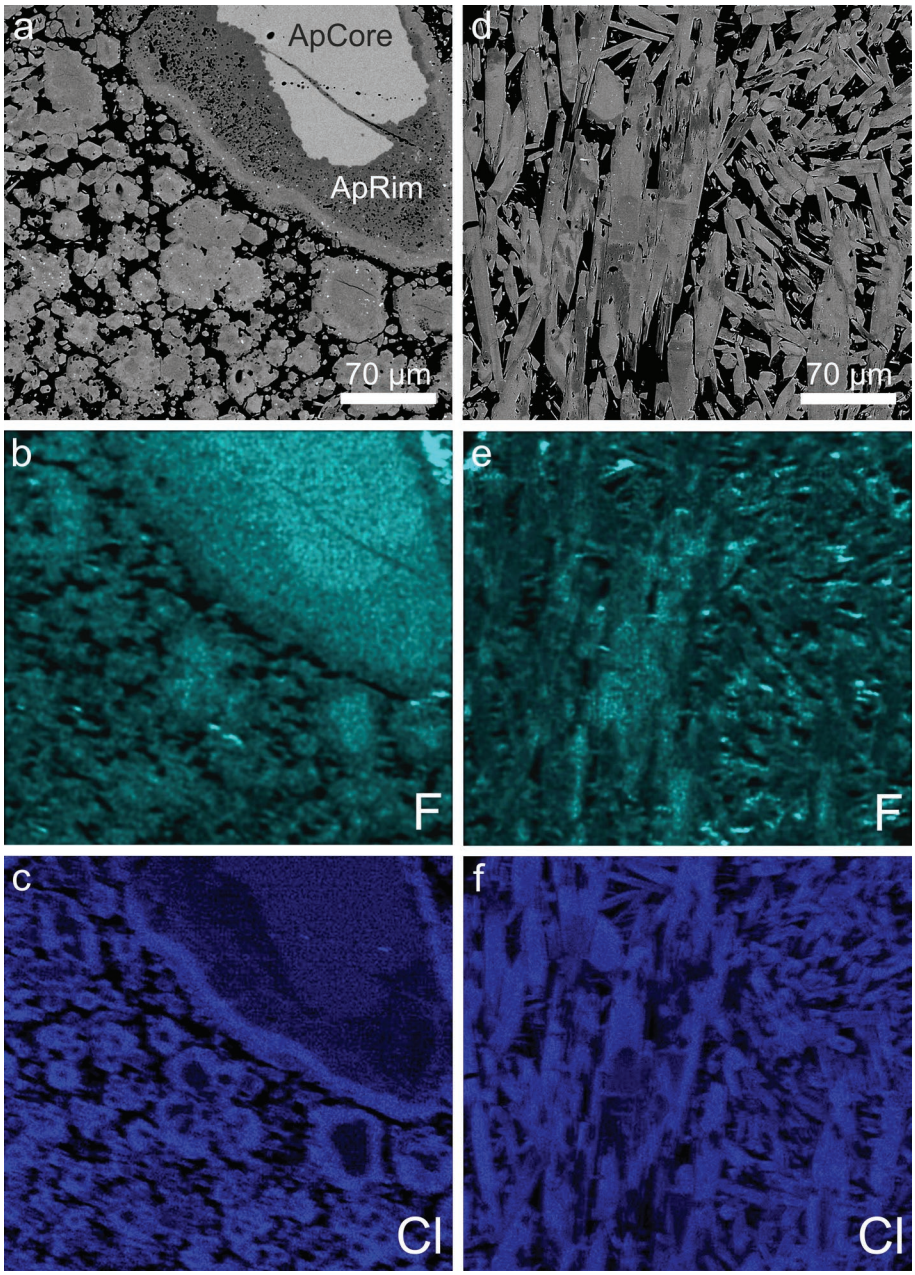

Fig. 6. BSE images and F and Cl distribution maps of fibrous apatites. **a** — A BSE image of a section perpendicular to *c* axis of a relict of core apatite (ApCore) embayed in a porous darker rim (ApRim) surrounded with fibrous apatite displaying concentric and patchy zoning and mottled structure. **b** — A fluorine distribution map illustrating F enrichment in core apatite (ApCore) and also in cores of concentric-zoned fibers. **c** — A chlorine distribution map showing Cl enrichment in rims of fibrous apatites appearing brighter than their cores in BSE images. **d** — A BSE image of a region in a section paralell to *c* axis of fibrous apatites showing patchy zoning and their mottled structure. **e** — A fluorine distribution map shows F enrichment mostly in regions darker in BSE. **f** — A chlorine distribution map illustrates Cl enrichment mostly in parts brighter in BSE.

Apatite crystallography

Povondra et al. (2007) speculated on the presence of monoclinic apatites in the fibrous material mantling the prismatic crystals. Their hypothesis was based on the interpretation of powder X-ray diffraction data acquired with a standard laboratory diffractometer. They also presented a precession photograph illustrating the unequivocally hexagonal symmetry of core apatite. Here, we confirmed the hexagonal symmetry of the core apatite using both single-crystal and powder X-ray diffraction. Single crystal data showed a considerable positional disorder in structure channels preventing a complete refinement of the F–Cl–(OH) assemblage; not only are the standard uncertainties of refined parameters excessively large, but the displacement parameters cannot be refined anisotropically. Once attempts to refine the ADPs are carried out, the result becomes crystallographically insensible leading to extremely elongated, mutually overlapping thermal ellipsoids along *c*-axis. Ultimately, such a positional disorder precludes the existence of a monoclinic phase, where channel anions are highly ordered. Single crystals of fibrous apatites display exactly the same behaviour;

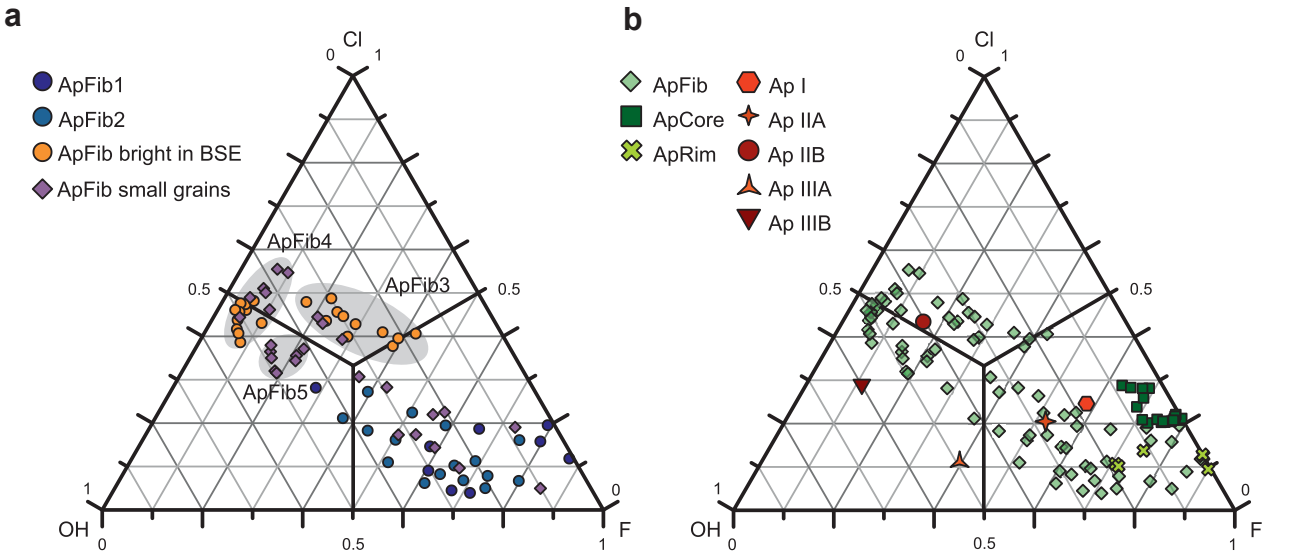

Fig. 7. Ternary diagrams of F, Cl and OH contents (in apfu) in distinct chemical and morphological types of apatites from this study and from the study of Povondra et al. (2007). **a** — A ternary diagram of F, Cl and OH contents (in apfu) in distinct chemical types of fibrous apatites. **b** — A ternary diagram comparing F, Cl and OH contents (in apfu) of all types of apatites from this study to those from Povondra et al. (2007) plotted in red colors.

they are hexagonal and their channel anions show a considerable disorder. We were also able to characterize a mixture of fibrous apatite from the mantles of the crystals using powder X-ray diffraction. It appeared that what Povondra et al. (2007) interpreted as a potential mixture of hexagonal and monoclinic phases is actually a much more complex mixture of hexagonal phases — in our particular case there were five apatite-structured phases with different unit-cell dimensions. Consequently, we may expect that monoclinic apatites are not present at the locality. We also believe that the high degree of positional disorder observed in apatites is linked to formation processes. Obviously, these processes must have been relatively fast, and the movement of fluids through the rock environment must have been turbulent to prevent the possible ordering of ions in the channel cavities in the apatite crystal structure.

Origin of the apatite assemblage and the host rock alteration minerals

A combination of the acquired data can help to shed light on the origin of the apatite assemblage and provide deeper characteristics of the alteration minerals found in the host rock. The hydrothermal origin of the apatite assemblage has already been suggested by Ďuďa et al. (1981) and Povondra et al. (2007). They concluded that the first mineral of the apatite assemblage to crystallize is the core apatite. This occurred during the post-magmatic stage, simultaneously with, or shortly after, the transformation of the original pyroxenes to amphiboles. The bright parts of core apatite are REE-, F- and Cl-rich. Halogens could be generally derived from marine sediments which probably originally occurred in the area and were pierced by intruding andesite host rock and partly resorbed in it as suggested by Černý et al. (1973). Then, the core apatite was partly dissolved and reprecipitated. This process is illustrated by the presence of darker patches in the BSE images along cracks of the crystals and darker regions at grain boundaries. Both these regions are chemically depleted in characteristics elements, mostly in LREE. This idea is also supported by the porous structure of darker parts and rarely observed inclusion trails. Similar porous and patchy zoning has been observed by many authors as a product of dissolution–reprecipitation or metasomatic processes (Harlov et al. 2002, 2005; Harlov 2015; Broom-Fendley et al. 2016; Krneta et al. 2017 and references therein). Many of these authors observed fine monazite and/or xenotime crystals in porous apatite; in our samples, however, only small amounts of ~1 μm-sized crystal were found rarely in ApRim zones and more often in the fibrous apatites. Several larger (~5 μm) inclusions of monazite were found in core apatite. In BSE images, darker and often porous areas are depleted in REE and Cl which is in agreement with the observation of Harlov et al. (2002, 2005). These parts are also depleted in Mg, Fe, Sr, Na and Si. Simultaneously with the dissolution of the core apatite, a decomposition of the original amphibole (edenite) and its replacement with actinolite-asbestos occurred. This is indicated by filling of the fractures of ApCore by actinolite-asbestos and also by rare occurrence of inclusions of actinolite fibres in fibrous apatites. Along with the coupled dissolution-reprecipitation of core apatite, crystallization of fibrous apatites followed. Compositional concentric and patchy zoning together with the presence of mottled structure in fibrous apatite reflect the formational process of this part of the apatite assemblage. We assume that the fibrous apatite which appeared bright in BSE images was the first of the fibrous apatites to form. BSE-bright fibrous apatites can be separated into three distinct types based on their chemistry: ApFib3, ApFib4 and

ApFib5. All these apatites are rich in Cl and OH and contain a relatively small, yet detectable (by Raman spectroscopy) amount of $(CO_3)^{2-}$ substituting phosphorus. Carbonate ions are not found in other types of apatite. This implies that these fluids formed by the dissolution of core apatite (enrichment of REE and Cl) and were further enriched in CO_2 and H_2O from another source. Porous and mottled structures observed in BSE images of dark parts of fibrous apatite grains indicate the action of another fluid dissolving fibrous apatites which appeared after the dissolution of core apatites. These dark parts are even more depleted in REE. Fibrous apatites darker in BSE images are rich in F with OH dominating over Cl. Small inclusions of monazite and Th-rich silicate were found in regions darker in BSE images where they deposited in micro-pores and presumable nano-voids (see e.g. Harlov et al. 2005). We suggest that CO_2 and REE with Cl were dissolved from apatite by an interaction with hydrothermal fluids and subsequently mobilized to form not only small inclusions but also xenomorphic grains of allanite. Allanites appear to be the youngest REE-bearing minerals formed in the host rock. Idiomorphic crystals with allanite in cores passing to epidote rims and oscillatory zoning in BSE-brighter parts of allanite and BSE-darker parts of epidote were rarely observed. Oscillatory zoning of repeated increase and decrease in REE contents in the epidote-group mineral grains could imply several hydrothermal events. Centres of prismatic idiomorphic crystals rich in REEs could indicate that they formed during the first event dissolving the core apatite most enriched in REEs. At the same time, the close association of xenomorphic epidote-group mineral grains with fibrous apatites implies that allanite could form from fluids derived from these apatite crystals. These observations can be explained by two different generations of their formation. Allanite does not belong among the products of dissolution–reprecipitation or metasomatism of REE-rich apatites. On the contrary, monazites and/or xenotime have been reported as a product of such processes in several papers — see above. Vanadium-rich Fe-oxides and Fe-sulphides rarely fill empty spaces between fibrous apatites or occur in cracks or form inclusions in core apatite indicating that they are possibly co-genetic with the base-metal mineralization known from the northern parts of the Slanské vrchy Mountains in a close proximity of Maglovec Hill (Ďuďa et al. 1981). However, it is beyond the purpose of this study to determinate the source of vanadium, which is also incorporated in the epidote-group minerals in small amounts. Replacement of plagioclases of intermediate composition with more albite-rich phase and compositional zoning observed in chlorites and micas further reinforce the idea of metasomatic event(s) as a feasible mechanism in the formation of the apatite assemblage at Maglovec Hill. We are not aware of a similar locality in the world.

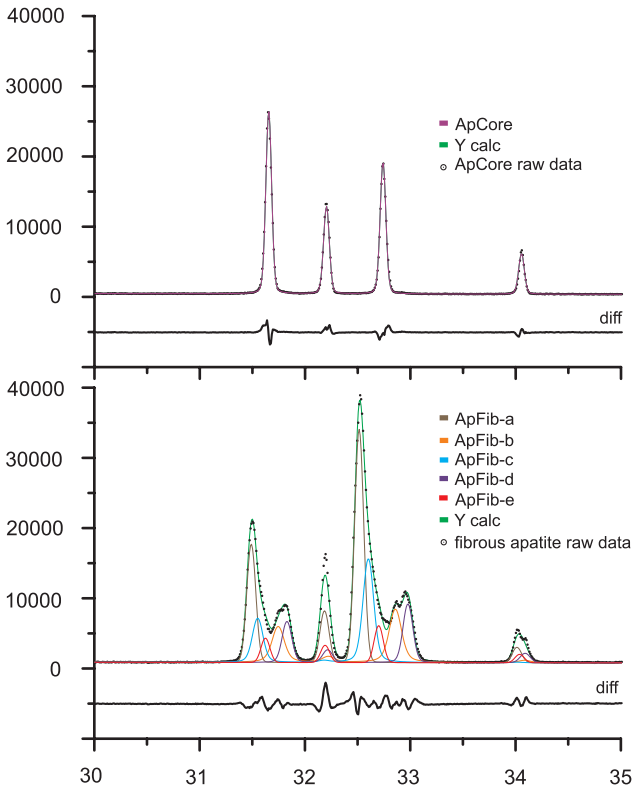

Fig. 8. Portions of a plot illustrating the results of the Rietveld refinement of powder X-ray diffraction data for core apatite and a sample consisting of a mixture of five individual apatite-structured phases; diff — a differential curve of raw data and the calculated model curve.

Conclusions

Two different morphological types of apatite were observed in the apatite assemblage from fissures of hydrothermally altered neovolcanic rocks (andesites and related lithologies) from Maglovec Hill (Slanské vrchy Mountains): apatite in cores of prismatic crystals and fibrous apatite rimming these cores. Core apatite (referred to as ApCore) is relatively homogeneous with some darker regions in the BSE images, which are developed mainly along fractures. It is rimmed with apatite of porous structure which is darker in the BSE images (ApRim). These rims further gradually pass into fibrous apatites. ApRim regions are depleted in trace elements, particularly in the LREE compared to the bright parts of ApCore. The dissolution–reprecipitation mechanism is suggested as the mechanism of formation of the darker parts of core apatite. Fibrous apatites vary in size significantly. Most grains display concentric and/or patchy zoning as well as mottled structure. This structure is caused by the differences in chemical composition, particularly in the variations in F and Cl contents. In general, fibrous apatites are depleted in trace element contents compared to both types of core apatite. Raman spectroscopy confirmed the presence of $(CO_3)^{2-}$ and/or OH in different populations of fibrous apatites. Combining the acquired data, we present our idea of the hydrothermal formation of this apatite assemblage. Neither single-crystal nor powder X-ray diffraction data provided a proof of monoclinic $P2_1/b$ symmetry among apatite samples from Maglovec Hill. Though the powder pattern of the sample taken from the layer of fibrous

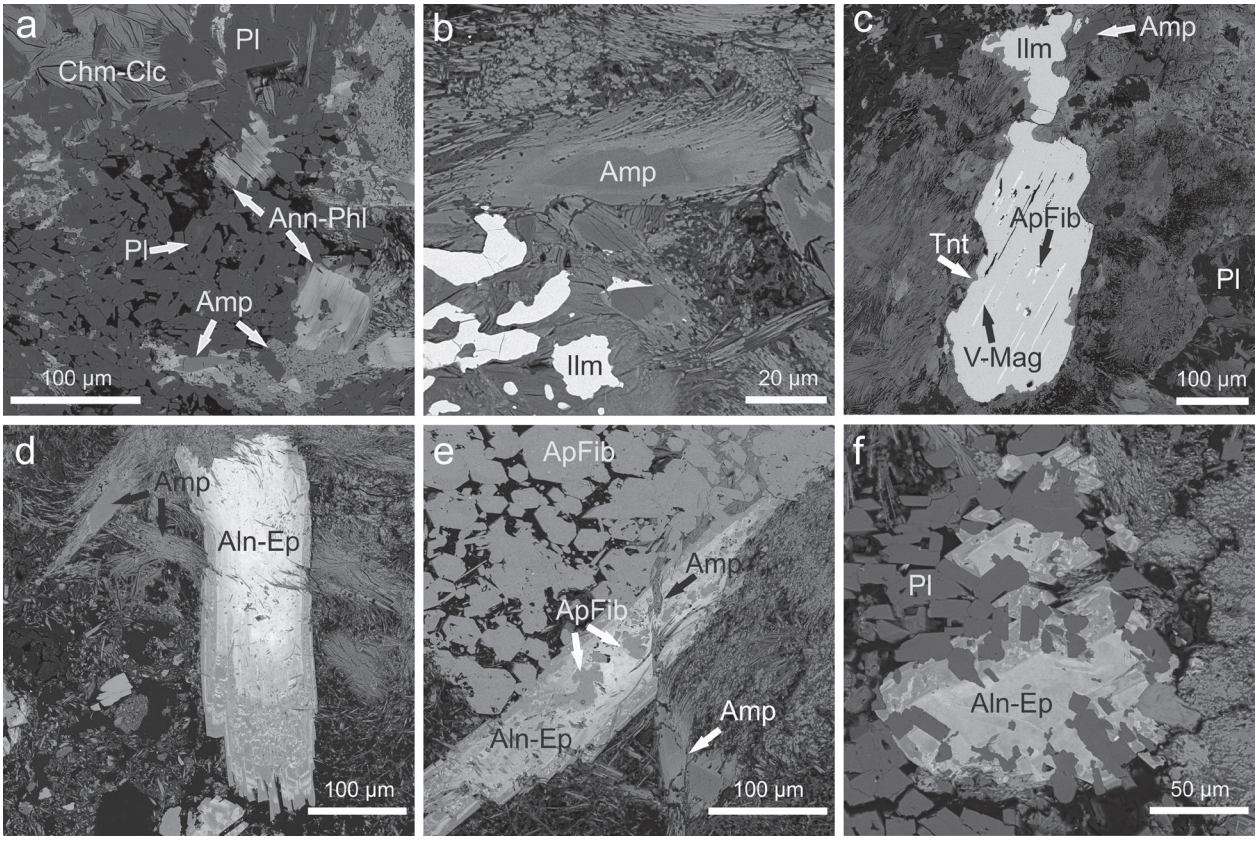

Fig. 9. Representative BSE images of host rock minerals. **a** — A BSE image illustrating two different plagioclase forms: xenomorphic grains in matrix and relicts of original hypidiomorphic bladed or tabular crystals. Matrix contains radial spherical aggregates of chlorite, solitary platy crystals of micas displaying significant patchy zoning and a relict of original amphibole decomposing to actinolite-asbestos which also fills some intergranular spaces. **b** — A close-up view of a relict of original amphibole decomposed to extremely fine fibrous actinolite-asbestos in a rare association with ilmenite xenomorphic grains. **c** — A hypidiomorphic ilmenite grain replaced by titanite along the edges with exsolution lamellae of vanadium-rich magnetite. **d** — A concentric- and oscillatory-zoned idiomorphic prismatic crystal of an epidote-group mineral. Brighter core corresponds to allanite, darker rims to epidote. The crystal is associated with spherules of chlorite and a relict of original amphibole decomposed to actinolite-asbestos. **e** — A grain of an epidote-group mineral embaying inclusions of fibrous apatite and actinolite-asbestos which also fills spaces between apatite crystals. **f** — A zoned xenomorphic grain of an epidote-group mineral filling intergranular spaces between individual crystals of plagioclases. Abbreviations: Amp — amphibole, ApFib — fibrous apatite, Aln-Ep — epidote-group minerals, Ann-Phl — annite-phlogopite, Chm-Clc — chamosite-clinochlore, Ilm — ilmenite, V-Mag — magnetite, Tnt — titanite, Pl — plagioclase.

apatites mantling yellow compact cores looked very complex, it was possible to fit the pattern with a mixture of 5 individual apatite-structured phases with hexagonal $P6_3/m$ symmetry. Compositional zoning in apatites with disordered distribution of channel anions in apatites substantiate the idea of multiple short-term metasomatic events which overlap both in time and place as a feasible mechanism in the formation of the apatite assemblage at Maglovec Hill. The hydrothermal origin is also supported by compositional zoning of other host rock minerals, especially by oscillatory compositional zoning of epidote-group minerals (allanite in cores rimmed with epidote) which are considered the youngest REE-bearing minerals formed in the host rock. Neither epidote-group minerals nor vanadium-rich magnetites have been described from this locality before.

Acknowledgements: This study was supported by the Institutional Research Plan No. RVO 67985831 of the Institute of Geology of the Czech Academy of Sciences, Prague. We thank anonymous reviewers for their constructive reviews as well as to editors M. Kohút and I. Broska for managing the manuscript. Later version of the manuscript benefited from comments by P. Bosák. Style and prose of the final version of the paper were improved by J. Adamovič.

References

Armbruster T., Bonazzi P., Akasaka M., Bermanec V., Chopin C., Gieré R., Heuss-Assbichler S., Liebscher A., Menchetti S., Pan Y. & Pasero M. 2006: Recommended nomenclature of epidote-group minerals. *Eur. J. Mineral*. 18, 5, 551–567.

Antonakos A., Liarokapis E. & Leventouri T. 2007: Micro-Raman and FTIR studies of synthetic and natural apatites. *Biomaterials* 28, 19, 3043–3054.

Awonusi A., Morris M.D. & Tecklenburg M.M.J. 2007: Carbonate assignment and calibration in the Raman spectrum of apatite. *Calcified Tissue International* 81, 1, 46–52.

Broom-Fendley S., Styles M.T., Appleton J.D., Gunn G. & Wall F. 2016: Evidence for dissolution-reprecipitation of apatite and preferential LREE mobility in carbonatite-derived late-stage hydrothermal processes. *Am. Mineral.* 101, 3, 596–611.

Bruker AXS 2008: TOPAS V4: General profile and structure analysis software for powder diffraction data. *User's Manual*, *Bruker AXS*, Karlsruhe, Germany.

Černý P., Parma Z., Povondra P. & Veselovský F. 1973: Occurence of danburite in xenolithes in andesite from Maglovec hill near Prešov. *Acta Universitatis Carolinae — Geologica* 1–2, 111–118 (in Czech).

Ďuďa R., Černý P., Kalinčiak M., Kalinčiaková E., Tözser J., Ulrych J. & Veselovský F. 1981: Mineralogy of northern part of Slánské vrchy Mountains. *Mineralia Slovaca, Monografia* 2, 1–99 (in Slovak).

Gaft M., Panczer G., Reisfeld R. & Uspesnsky E. 2001: Laser-induced time-resolved luminescene as a tool for rare-earth element identification in minerals. *Phys. Chem. Miner.* 28, 5, 347–363.

Goldoff B., Webster J.D. & Harlov D.E. 2012: Characterization of fluor-chlorapatites by electron probe microanalysis with a focus on time-dependent intensity variation of halogens. *Am. Mineral.* 97, 7, 1103–1115.

Guggenheim S., Adams J.M., Bain D.C., Bergaya F., Brigatti M.F., Drits V.A., Formoso M.L.L., Galán E., Kogure T. & Stanjek H. 2006: Summary of recommendations of nomenclature committees relevant to clay mineralogy: report of the Association Internationale Pour L'Etude Des Argiles (AIPEA) nomenclature committee for 2006. *Clays Clay Miner*. 54, 761–772.

Harlov D.E. 2015: Apatite: A Fingerprint for Metasomatic Processes. *Elements* 11, 3, 171–176.

Harlov D.E., Förster H.J. & Nijland T.G. 2002: Fluid-induced nucleation of (Y+REE)-phosphate minerals within apatite: Nature and experiment. Part I. Chlorapatite. *Am. Mineral.* 87, 245–261.

Harlov D.E., Wirth R. & Förster H. J. 2005: An experimental study of dissolution-reprecipitation in fluorapatite: Fluid infiltration and the formation of monazite. *Contrib. Mineral. Petrol.* 150, 3, 268–286.

Hawthorne F.C., Oberti R., Harlow G.E., Maresch W.V., Martin R.F., Schumacher J.C. & Welch M.D. 2012: Ima report: Nomenclature of the amphibole supergroup. *Am. Mineral.* 97, 11–12, 2031–2048.

Hughes J.M., Cameron M. & Crowley K.D. 1989: Structural variations in natural F, OH, and Cl apatites. *Am. Mineral.* 74, 870–876.

Jochum K.P., Weis U., Stoll B., Kuzmin D., Yang Q., Raczek I., Jacob D.E., Stracke A., Birbaum K., Frick D.A., Günther D. & Enzweiler J. 2011: Determination of reference values for NIST SRM 610-617 glasses following ISO guildelines. *Geostand. Geoanal. Res*. 35, 397–429.

Klemme S., Prowatke S., Münker C., Magee C.W., Lahaye Y., Zack T., Kasemann S.A., Cabato E.J. A. & Kaeser B. 2008: Synthesis and preliminary characterisation of new silicate, phosphate and titanite reference glasses. *Geostand. Geoanal. Res*. 32, 1, 39–54.

Krneta S., Ciobanu C.L., Cook N.J., Ehrig K. & Kontonikas-Charos A. 2017: Rare Earth Element Behaviour in Apatite from the Olympic Dam Cu–U–Au–Ag Deposit, South Australia. *Minerals* 7, 8, 135.

Kuthan M. 1948: The undation volcanism of the. Carpathian orogene and volcanological survey of the northem part of the Prešov Mountains. *Geologické práce — Zošit* 17, 87–174 (in Slovak).

Lafuente B., Downs R.T., Yang H. & Stone N. 2015: The power of databases: the RRUFF project. In: Armbruster T. & Danisi R.M. (Eds.): Highlights in Mineralogical Crystallography. *W. De Gruyter,* Berlin, 1–30.

Lenz C. & Nasdala L. 2015: A photoluminescence study of REE^{3+} emissions in radiation-damaged zircon. *Am. Mineral.* 100, 1123–1133.

MacRae C.M. & Wilson N.C. 2008: Luminescence Database I — Minerals and Materials. *Microsc. Microanal.* 14, 2, 184–204.

Marcinčáková Z. & Košuth M. 2011: Characteristics of Xenoliths in the East Slovakian Neogene Volcanites. *Al. I. Cuza " Din Iasi Seria Geologie* 57, 1, 17–27.

O'Donnell M.D., Hill R.G., Law R.V. & Fong S. 2009: Raman spectroscopy, ^{19}F and ^{31}P MAS-NMR of a series of fluorochloroapatites. *Journal of the European Ceramic Society* 29, 377–384.

Pan Y. & Fleet M.E. 2002: Compositions of the Apatite-Group Minerals: Substitution Mechanisms and Controlling Factors. *Rev. Mineral. Geochem.* 48, 1, 13–49.

Pasero M., Kampf A. R., Ferraris C., Pekov I. V., Rakovan J., & White T. J. 2010: Nomenclature of the apatite supergroup minerals. *Eur. J. Mineral.* 22, 2, 163–179.

Penel G., Leroy G., Rey C., Sombret B., Huvenne J.P. & Bres E. 1997: Infrared and Raman microspectrometry study of fluor-fluor-hydroxy and hydroxy-apatite powders. *J. Mater. Sci. — Mater. Med.* 8, 5, 271–276.

Penel G., Leroy G., Rey C. & Bres E. 1998: MicroRaman spectral study of the PO_4 and CO_3 vibrational modes in synthetic and biological apatites. *Calcified Tissue International* 63, 6, 475–481.

Petříček V., Dušek M. & Palatinus L. 2014: Crystallographic Computing System JANA2006: General features. *Zeitschrift Für Kristallographie* 229, 5, 345–352.

Plissart G., Féménias O., Mãruntiu M., Diot H. & Demaiffe D. 2009: Mineralogy and geothermometry of gabbro-derived listvenites in the Tisovita-Iuti ophiolite southwestern Romania. *Canad. Mineral.* 47, 81–105.

Povondra P., Skála R. & Chapman R. 2007: Hydrothermal assemblage of Cl–F- and OH-bearing apatite-group minerals from Maglovec near Prešov, Slovakia. *Canad. Mineral.* 45, 6, 1355–1366.

Rieder M., Cavazzini G., Yakonov Y.D., Frank-Kanetskii V.A., Gottardi G., Guggenheim S., Koval P.V., Muller G., Neiva A.M.R., Radoslovich E.W., Robert J.L., Sassi F.P., Takeda H., Weiss Z. & Wones D.R. 1998: Nomenclature of the micas. *Canad. Mineral.* 36, 3, 905–912.

Stock M.J., Humphreys M.C.S., Smith V.C., Johnson R.D. & Pyle D.M. 2015: New constraints on electron-beam induced halogen migration in apatite. *Am. Mineral.* 100, 1, 281–293.

Stormer J.C., Pierson M.L. & Tackler R.C. 1993: Variation of F and Cl X-ray intensity due to anisotropicdiffusion in apatite during electron microprobe analysis. *Am. Mineral.* 78, 641–648.

Tacker C.R. 2004: Hydroxyl ordering in igneous apatite. *Am. Mineral.* 89, 1411–1421.

Tischendorf G., Gottesmann B., Förster H.J. & Trumbull R.B. 1997: On Li-bearing micas: estimating Li from electron microprobe analyses and improved diagram for graphical representation. *Mineral. Mag.* 61, 6, 809–834.

van Achterbergh E., Ryan C.G., Jackson S.E. & Griffin W. 2001: Data reduction software for LA-ICPMS. In: Sylvester P. (Ed.): Laser Ablation ICPMS in the earth sicence: principles and applications. *Mineral. Ass. Canada* 29, 239–243.

Wang A., Kuebler K.E., Jolliff B.L. & Haskin L.A. 2004: Raman spectroscopy of Fe–Ti–Cr-oxides, case study: Martian meteorite EETA79001. *Am. Mineral.* 89, 665–680.

Waychunas G.A. 2002: Apatite Luminescence. *Rev. Mineral. Geochem*. 48, 1, 701–742.

Wojdyr M. 2010: Fityk: a general-purpose peak fitting program. *J. Appl. Crystallogr*. 43, 1126–1128.

Zane A. & Weiss Z. 1998: A procedure for classifying rock-forming chlorites based on microprobe data. *Rendiconti Lincei-Scienze Fisiche E Naturali*. 9, 51–56.

Supplement

Determination of major element compositions of minerals

Major element concentrations were obtained by a CAMECA SX-100 electron probe microanalyzer (EPMA) equipped with four wavelength-dispersive X-ray spectrometers, at the Department of Analytical Methods, Czech Academy of Sciences, Institute of Geology, Prague. To analyze epidote-group minerals the accelerating voltage of 15 kV, the sample current of 20 nA and an electron beam of 2 μm diameter were applied. For analyses of ilmenites and other silicates the accelerating voltage of 15 kV, the sample current of 10 nA, and an electron beam of 2 μm diameter were applied. Focused beam was used for the measurement of grain too small to use a 2μm beam spot; all other conditions remained unchanged in these cases.

For **silicate** minerals (e.g., amphibole, plagioclases, chlorites) the analyzed elements included (spectral line, spectrometer crystal, standard, detection limit in ppm, respectively are given in parentheses): F (*Kα*, PC0, fluorite, 1322), Na (*Kα*, TAP, jadeite, 338), Mg (*Kα*, TAP, periclase, 423), Al (*Kα*, TAP, jadeite, 210), Si (*Kα*, TAP, quartz, 340), P (*Kα*, LPET, apatite, 281), Cl (*Kα*, LPET, tugtupite, 338), K (*Kα*, LPET, sanidine, 262), Ca (*Kα*, LPET, diopside, 332), Ti (*Kα*, LPET, rutile, 214), Mn (*Kα*, LIF, rhodonite, 962), Fe (*Kα*, LIF, hematite, 1220).

For **ilmenites** the analyzed elements included: F (*Kα*, PC0, fluorite, 1402), Mg (*Kα*, TAP, periclase, 388), Al (*Kα*, TAP, jadeite, 296), Si (*Kα*, TAP, quartz, 294), P (*Kα*, LPET, apatite, 194), Ca (*Kα*, LPET, diopside, 223), Ti (*Kα*, LPET, rutile, 331), V (*Kα*, LLIF, V_2O_5, 789), Cr (*Kα*, LLIF, Cr_2O_3, 651), Mn (*Kα*, LLIF, Mn spinel, 832), Fe (*Kα*, LLIF, hematite, 1675), La (*Lα*, LLIF, monazite, 1635), Ce (*Lα*, LLIF, monazite, 2063).

For **epidote-group** minerals the analyzed elements included: F (not detected), Mg (*Kα*, TAP, periclase, 251), Al (*Kα*, TAP, jadeite, 254), Si (*Kα*, TAP, quartz, 341),Ca (*Kα*, LPET, diopside, 266), V (*Kα*, LLIF, V, 542), Cr (*Kα*, LLIF, Cr_2O_3, 618), Mn (*Kα*, LLIF, Mn spinel, 622), Fe (*Kα*, LLIF, magnetite, 1120), Sr (*Lα*, LPET, celestite, 487), Y (*Lα*, LPET, Y-Al garnet, 449), La (*Lα*, LLIF, monazite, 1276), Ce (*Lα*, LLIF, monazite, 1539), Pr (*Lβ*, LLIF, monazite, 4811), Nd (*Lα*, LLIF, monazite, 1335), Pb (*Mα*, LPET, crocoite, 703), Th (*Mβ*, LPET, Th REE glass, 1257).

Calculation of empirical formulae

Plagioclase formulae were recalculated based on 8 oxygens per formula unit. WinCcac software (Yavuz at al. 2015) was used to calculate and classify analyses of chlorites. Empirical formulae and classification of micas were performed with Mica$^+$ software (Yavuz 2003). Analyses of amphibole supergroup minerals were recalculated using the program by Locock (2014). Calculation of empirical formulae of minerals of epidote-group minerals included the calculation of FeO and Fe_2O_3 amounts followed by a recalculation based on 8 cations per formula unit as suggested by Armbruster et al. (2006). All analyses of ilmenites were recalculated based on 3 oxygen atoms per formula unit and all analyses of titanites were recalculated based on 5 oxygen atoms per formula unit. The calculations of magnetite empirical formulae included the alculation of the FeO and Fe_2O_3 followed by recasting the formulae to 3 cations.

References

Armbruster T., Bonazzi P., Akasaka M., Bermanec V., Chopin C., Gieré R., Heuss-Assbichler S., Liebscher A., Menchetti S., Pan Y. & Pasero M. 2006: Recommended nomenclature of epidote-group minerals. *Eur. J. Mineral*. 18, 5, 551–567.

Locock A.J. 2014: An Excel spreadsheet to classify chemical analyses of amphiboles following the IMA 2012 recommendations. *Computers and Geosciences* 62, 1–11.

Yavuz F. 2003: Evaluating micas in petrologic and metallogenic aspect: I-definitions and structure of the computer program MICA+. *Computers and Geosciences* 29, 10, 1203–1213.

Yavuz F., Kumral M., Karakaya N., Karakaya M.T., & Yildirim D.K. 2015: A Windows program for chlorite calculation and classification. *Computers and Geosciences* 81, 101–113.

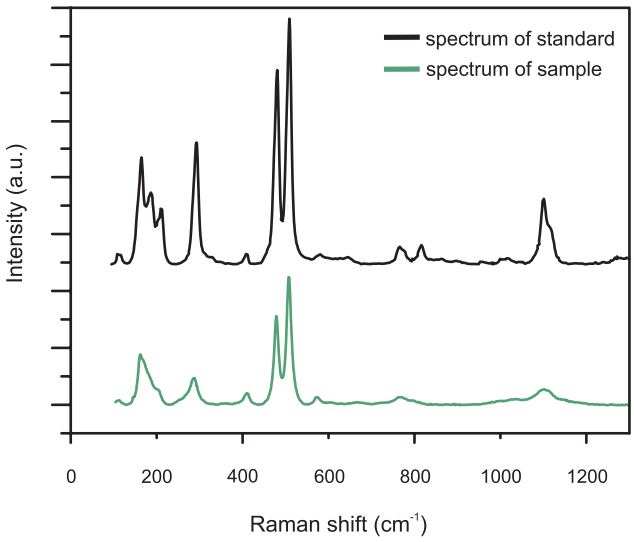

Fig. S1. A representative Raman spectrum of plagioclase compared to the spectrum from RRUFF database.

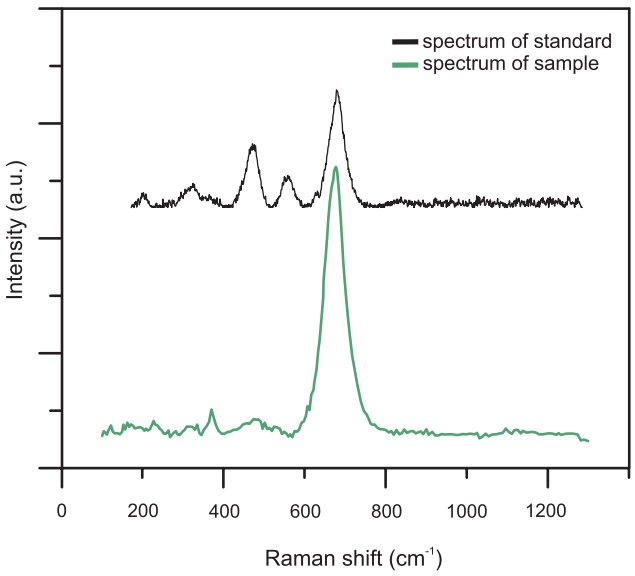

Fig. S2. A representative Raman spectrum of magnetite compared to the spectrum from RRUFF database.

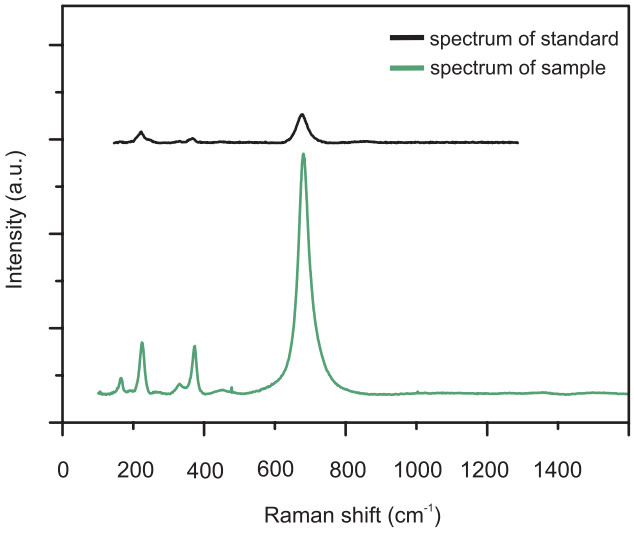

Fig. S3. A representative Raman spectrum of ilmenite compared to the spectrum from RRUFF database.

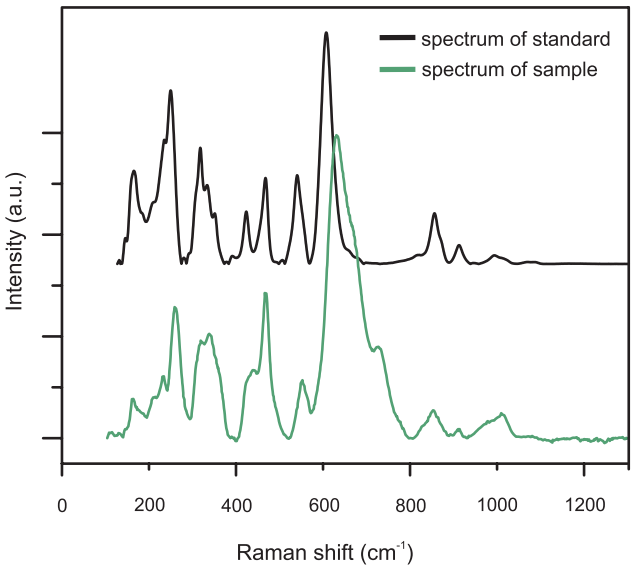

Fig. S4. A representative Raman spectrum of titanite compared to the spectrum from RRUFF database.

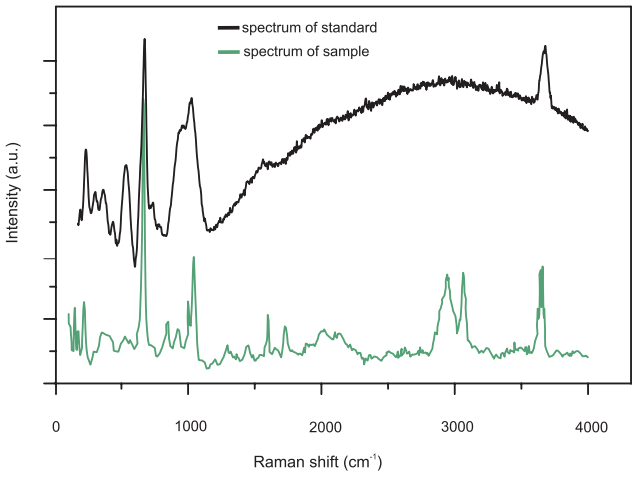

Fig. S5. A representative Raman spectrum of actinolite-asbestos compared to the actinolite spectrum from RRUFF database. Additional peaks in the sample spectrum are due to epoxy resin.

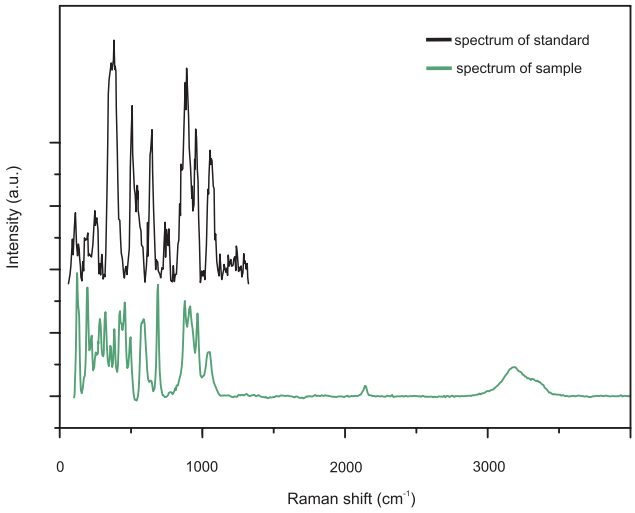

Fig. S6. A representative Raman spectrum of allanite (BSE-bright core of epidote-group mineral grains) compared to the spectrum from RRUFF database.

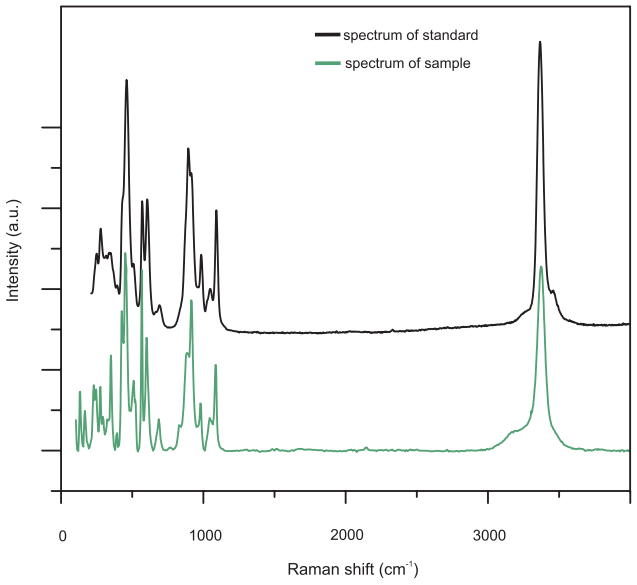

Fig. S7. A representative Raman spectrum of epidote (BSE-dark regions of epidote-group mineral grains) compared to the spectrum from RRUFF database.

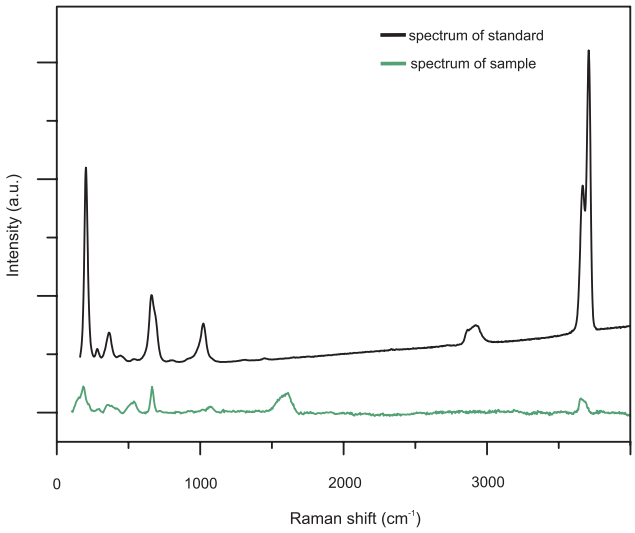

Fig. S8. A representative Raman spectrum of annite (dark regions of mica platy crystals) compared to the spectrum from RRUFF database.

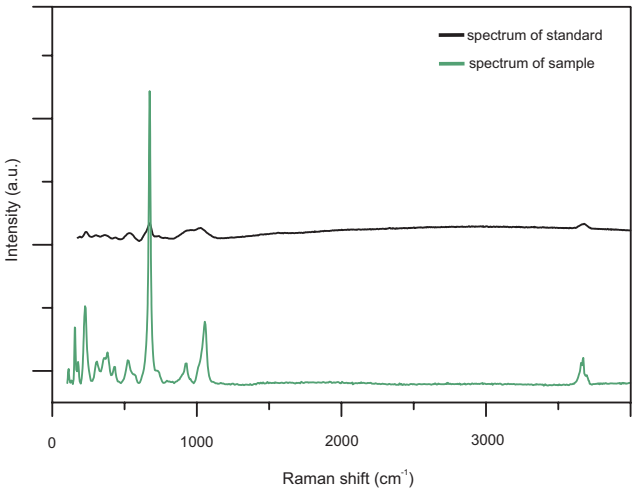

Fig. S9. A representative Raman spectrum of edenite (relicts of original amphibole) compared to the spectrum from RRUFF database.

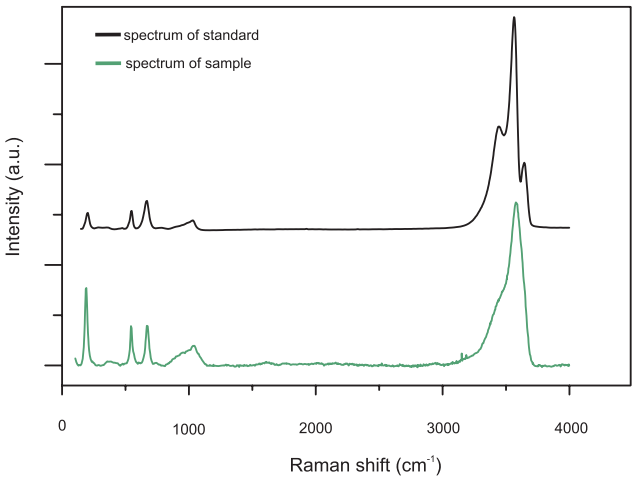

Fig. S10. A representative Raman spectrum of a chlorite group mineral compared to the chamosite spectrum from RRUFF database.

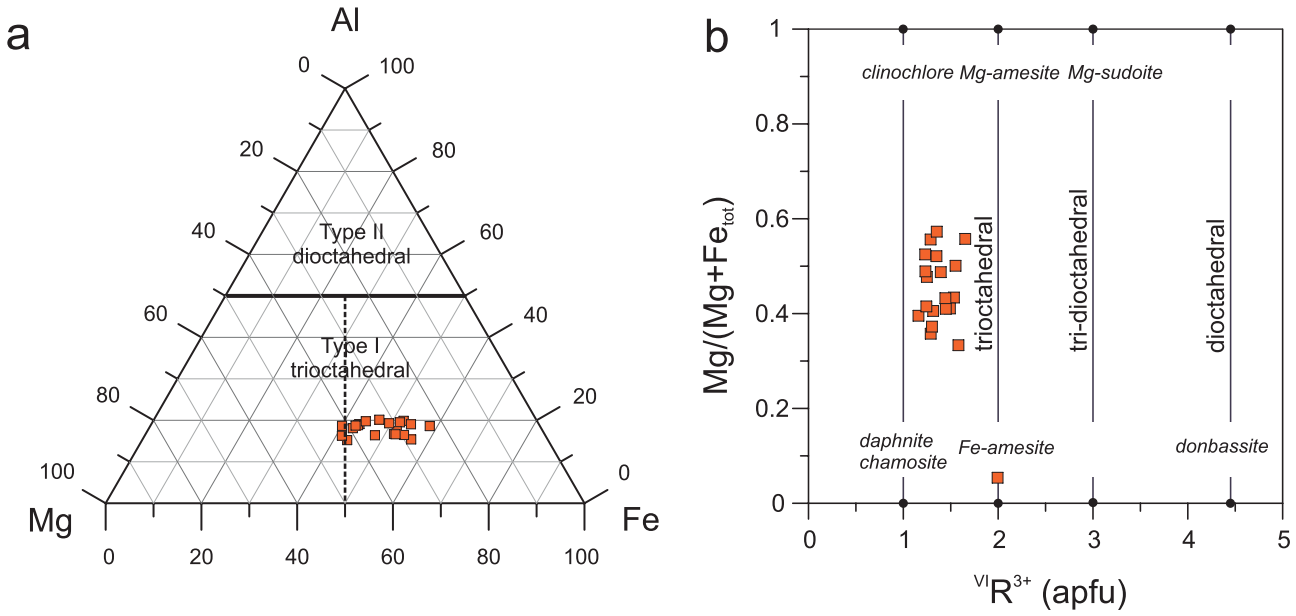

Fig. S11. Classification diagrams of chlorites from the Maglovec locality. Diagram (**a**) is taken from Zane & Weiss (1998) and (**b**) from Plissart et al. (2009).

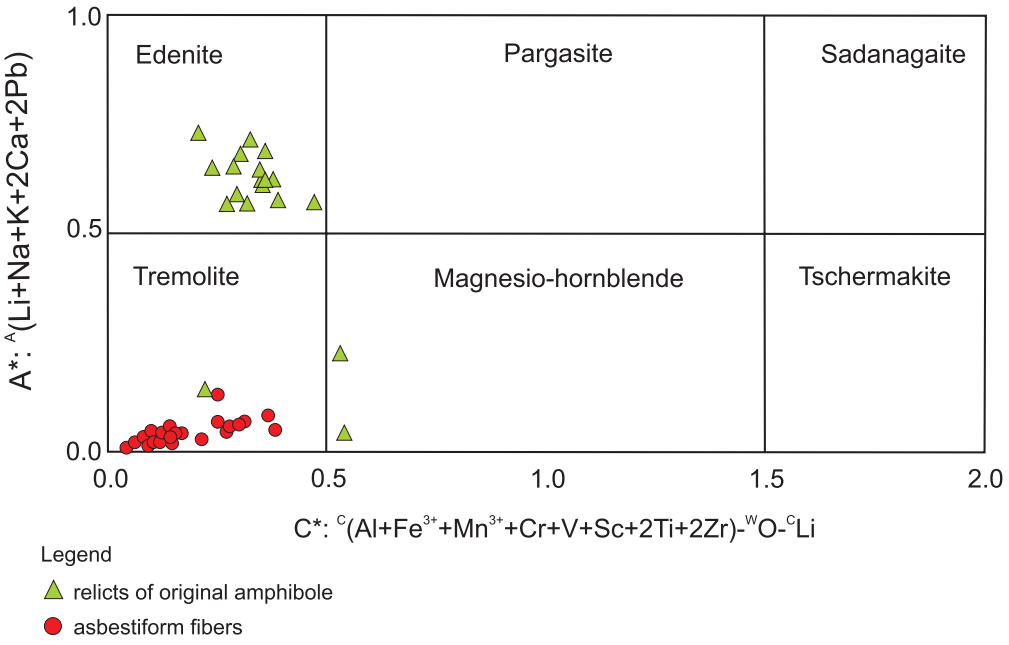

Fig. S12. A classification diagram of amphiboles (asbestos and relicts of original amphiboles) from the Maglovec locality. The diagram is taken from Hawthorne et al. (2012).

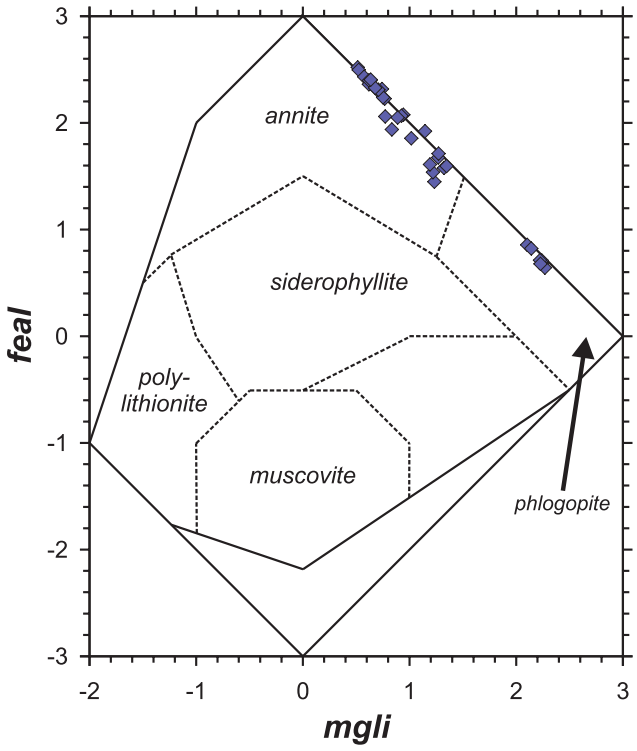

Fig. S13. A simplified classification diagram *feal* vs. *mgli* of micas from the Maglovec locality. The diagram is taken from Tischendorf et al. (1997).

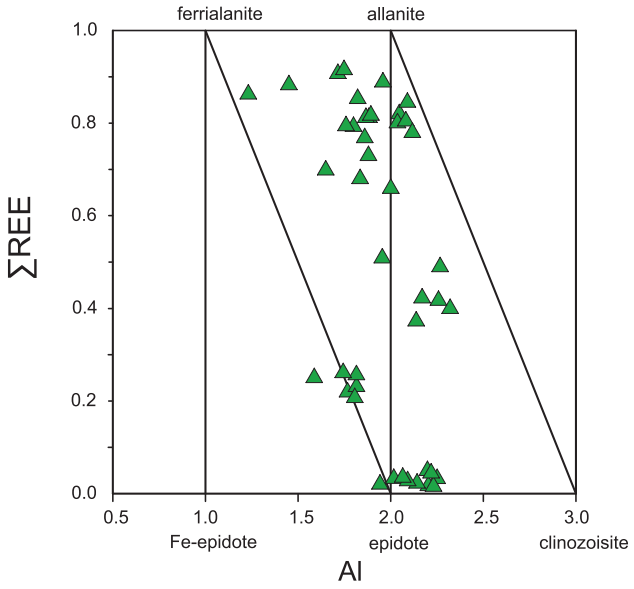

Fig. S14. A classification diagram of epidote-group minerals from the Maglovec locality.

Table S1: Trace element concentrations in BSE brighter (ApCore) and darker (ApRim) regions of core and fibrous apatite (ApFib), given in ppm.

Sample	Li	B	V	Mn	Rb	Sr	Y	Zr	Nb	Sb	Cs	Ba	La	Ce	Pr	Nd	Sm	Eu	Gd	Tb	Dy	Ho	Er	Tm	Yb	Lu	Hf	Pb	Th	U
ApCore-10b	3.4	5.4	n.a.	n.a.	0.11	654	1825	12	b.d.l.	0.046	b.d.l.	8.5	4197	7392	919	3364	583	31	597	78	427	80	200	23	120	16	0.052	0.94	1118	32
ApCore-11b	b.d.l	6.6	n.a.	n.a.	0.18	631	1810	11	0.12	0.26	b.d.l.	8.0	4208	7355	919	3292	597	31	587	76	404	75	192	23	120	15	0.081	0.97	1091	32
ApCore-14a	2.4	15.4	n.a.	n.a.	0.12	716	1632	9	b.d.l.	0.071	b.d.l.	17	5432	10327	1155	3403	547	29	496	61	327	59	147	16	86	11	0.055	1.4	1114	38
ApCore-15a	3.2	14.1	n.a.	n.a.	0.14	740	1578	9	b.d.l.	0.077	b.d.l.	18	5803	11850	1261	3465	555	31	529	65	359	66	167	19	101	13	0.081	1.3	1105	42
ApCore-20c	b.d.l	9.7	n.a.	n.a.	0.61	619	1278	10	0.12	b.d.l.	b.d.l.	11	4301	7658	839	2608	464	25	412	50	259	48	122	15	80	10	b.d.l.	0.72	739	30
ApCore-21c	2.7	11	n.a.	n.a.	0.14	633	1335	10	0.070	b.d.l.	b.d.l.	9.9	4389	6982	838	2642	473	27	418	53	276	51	132	15	80	10	0.050	0.70	768	29
ApCore-15	b.d.l	6.5	21	351	0.19	642	1747	8	b.d.l.	b.d.l.	b.d.l.	9.1	4469	8241	997	3546	613	30	576	75	404	74	186	21	114	14	0.086	1.3	1153	43
ApCore-16	4.1	13.7	23	362	0.18	701	1976	8.5	b.d.l.	b.d.l.	b.d.l.	14	4924	9427	1096	3661	610	27	558	74	388	70	181	21	122	15	0.16	1.4	1428	47
ApCore-18	5.6	8.7	26	381	1.4	641	1880	11	0.18	b.d.l.	0.103	11	4273	8404	1089	3618	618	33	619	79	399	74	183	22	123	16	0.13	1.6	1382	56
ApCore-19	b.d.l	13.6	27	381	b.d.l.	625	1487	11	b.d.l.	b.d.l.	b.d.l.	13	5015	8257	961	3387	600	32	519	66	343	66	163	18	99	12	b.d.l.	0.97	1012	49
ApCore-20	b.d.l	13.9	25	358	0.24	645	1844	12	0.12	0.043	b.d.l.	10	5562	8872	1020	3686	607	29	560	75	399	80	197	23	119	16	0.104	1.5	1542	43
ApRim-17	b.d.l	4.1	9.5	109	0.57	197	1045	20	0.21	7.0	0.096	2.3	299	1197	204	963	255	16	280	38	230	44	108	12	61	7.4	0.21	8.6	1349	41
ApRim -18a	2.2	2.6	n.a.	n.a.	0.13	267	530	3.9	b.d.l.	0.047	0.038	1.3	874	2493	312	951	181	13	183	23	126	25	64	7	38	4.6	0.045	0.89	726	28
ApRim -19a	b.d.l	2.4	n.a.	n.a.	0.14	282	858	9.2	0.10	0.40	b.d.l.	3.2	934	3002	398	1387	283	18	272	38	202	36	94	11	52	6.0	0.075	1.0	955	20
ApRim -8a	b.d.l	b.d.l.	n.a.	n.a.	0.10	175	811	11	0.092	1.1	0.15	1.4	175	648	122	579	164	11	186	28	152	30	77	8,6	42	4.7	0.092	3.3	542	10
ApRim -8b	b.d.l	1.7	n.a.	n.a.	0.20	194	977	8.2	0.087	0.63	0.048	1.4	239	889	160	735	211	13	231	34	186	37	87	10	50	5.6	0.071	1.7	596	10
ApFib-21	b.d.l	b.d.l.	b.d.l.	145	b.d.l.	300	1087	6.7	0.24	0.10	0.08	1.0	470	1378	241	1077	275	20	301	42	226	43	113	12	57	5.7	0.054	0.64	350	19
ApFib -22a	b.d.l	b.d.l.	2.0	155	b.d.l.	286	1326	3.9	0.071	0.18	b.d.l.	1.0	640	2268	372	1546	374	21	428	56	296	57	136	17	88	9.8	0.027	0.41	393	11
ApFib -23a	b.d.l	b.d.l.	0.9	157	0.16	181	922	11	b.d.l.	0.12	0.095	2.7	173	519	95	515	166	13	219	32	181	37	90	10	40	3.6	0.12	1.2	1534	45
ApFib -26b*	3.3	13	7.6	214	0.20	539	1818	8.7	0.20	b.d.l.	b.d.l.	8.7	4220	6836	782	2846	548	26	530	69	371	72	177	21	110	14	0.14	1.3	1588	44
ApFib -27b	b.d.l	3.4	b.d.l.	160	b.d.l.	253	1834	7.8	0.38	0.33	b.d.l.	1.5	518	1772	326	1479	422	41	489	67	367	72	170	20	93	10	0.11	1.0	1131	38
ApFib -29b	b.d.l	8.6	0.64	164	b.d.l.	244	1038	22	0.14	1.9	b.d.l.	0.73	553	1801	284	1172	270	10	283	38	214	43	108	13	61	8.0	0.24	4.1	1166	43
ApFib -30	b.d.l	b.d.l.	b.d.l.	131	0.26	292	1243	11	0.19	0.28	b.d.l.	1.2	636	2292	374	1656	408	19	406	54	288	54	129	15	75	8.0	0.11	0.61	729	49
ApFib -32	b.d.l	8	3.1	160	0.16	271	1511	3.5	0.086	4.6	b.d.l.	1.2	1032	3512	554	2348	552	16	537	67	335	63	151	17	85	10	b.d.l.	1.1	785	22
ApFib -4	b.d.l	3.6	n.a.	n.a.	b.d.l.	258	1065	2.0	0.075	2.0	b.d.l.	0.64	715	2185	399	1794	358	13	338	46	242	43	103	12	54	6.0	0.025	0.49	356	10
ApFib -5	b.d.l	2.7	n.a.	n.a.	0.14	289	1440	9.4	0.11	0.51	0.10	0.73	616	1978	366	1682	367	16	374	53	286	55	140	16	79	8.7	0.040	0.67	586	18
ApFib -6	b.d.l	3.1	n.a.	n.a.	0.13	323	1059	2.7	0.16	0.43	b.d.l.	0.97	588	1852	307	1313	279	15	274	39	215	40	122	12	61	6.7	b.d.l.	0.47	251	7
ApFib -7	b.d.l	3.8	n.a.	n.a.	b.d.l.	286	1300	3.9	0.13	2.4	b.d.l.	1.1	870	2806	507	2158	424	15	409	54	280	52	127	14	70	7.7	0.065	0.58	537	17
ApFib -16	b.d.l	3.1	n.a.	n.a.	0.20	262	1545	7.5	0.11	0.56	b.d.l.	0.49	651	2243	421	1716	418	19	421	58	312	57	149	17	83	9.8	0.065	1.2	962	29
ApFib -17	2.1	2.2	n.a.	n.a.	b.d.l.	259	1353	2.0	0.12	0.40	b.d.l.	1.3	483	1950	307	1319	323	20	338	47	265	49	124	15	69	7.7	0.060	0.28	217	11
ApFib -22b	b.d.l	1.9	n.a.	n.a.	0.10	325	1116	9.3	b.d.l.	0.19	0.48	0.38	557	1634	276	1138	273	18	306	41	223	42	113	13	61	6.9	b.d.l.	0.56	548	21
ApFib -23b	b.d.l	2.4	n.a.	n.a.	0.13	304	1209	9.6	0.084	0.078	b.d.l.	0.75	554	1736	286	1206	293	20	312	43	236	45	117	13	64	7.5	0.072	0.49	595	16
ApFib -26a*	2.8	10	n.a.	n.a.	0.15	604	1996	9.6	0.088	b.d.l.	0.043	10	5638	8998	1065	3296	607	26	575	74	391	74	195	23	123	16	0.11	0.97	1337	28
ApFib -27a	b.d.l	1.5	n.a.	n.a.	0.15	222	2267	10	b.d.l.	0.183	b.d.l.	0.79	412	1604	315	1514	478	46	563	79	428	80	203	23	101	9.8	b.d.l.	0.79	1138	30
ApFib -28a	b.d.l	2.3	n.a.	n.a.	0.17	241	1429	13	b.d.l.	0.191	b.d.l.	0.67	434	1421	255	1121	326	33	366	55	269	51	127	14	71	7.5	b.d.l.	0.74	895	24
ApFib -29a	b.d.l	2	n.a.	n.a.	0.10	265	1429	11	0.063	0.95	b.d.l.	0.93	503	1608	292	1176	331	26	364	51	273	53	133	15	72	8.0	0.059	0.98	1410	49

Explanatory notes: b.d.l. — below detection limits; n.a. — not analyzed; ApCore — bright regions of core apatite; ApRim — dark parts of core apatite; ApFib — fibrous apatite; * — analyses of zonality in fibrous apatite chemically closely resembling core apatite

Table S2: Crystal structure data refined from single-crystal X-ray diffraction data of core and fibrous apatite and powder X-ray diffraction of core apatite (last column).

	Core apatite	**Fibrous apatite**	**Core apatite**	**Fibrous apatite**	**Core apatite**
***a* (Å)**	9.4367(6)	9.4341(14)	9.4690(2)	9.44000(10)	9.4632(2)
***c* (Å)**	6.8607(4)	6.8737(14)	6.8550(2)	6.86500(10)	6.85623(17)
***V* (Å^3)**	529.10(9)	529.81(15)	532.29(2)	529.804(11)	531.73(3)
***D*$_{calc}$ (g/cm^3)**	3.162	3.1335	3.1488	3.1623	3.114(6)
Diffractometer	Rigaku SuperNova, AtlasS2		Nonius Kappa CCD		Bruker D8 Discover
Radiation	Mo$K\alpha$				Cu$K\alpha_1$
Crystal dimensions (mm)	0.107×0.056×0.052		0.552×0.321×0.207	0.210×0.144×121	powder
Limiting theta angles (°)	3.88–28.18	3.87–29.64	2.48–27.45	2.49–27.45	4–70.04
Limiting Miller indices	−12 : 12 ; −12 : 12 ; −8 : 9	−11 : 11 ; −11 : 11 ; −8 : 8	−12 : 12 ; −12 : 12 ; −8 : 8	−12 : 12 ; −12 : 12 ; −8 : 8	0 : 11 ; 0 : 11 ; 0 : 8
No. of reflections	6586	3165	12366	12621	373
No. of unique reflections	458	478	443	442	
No. of observed reflections	430	335	262	303	
***μ* (mm^{-1})**	3.115	3.056	3.036	3.092	26.74
***T*$_{min}$/*T*$_{max}$**	0.78/0.89	0.259/1	0.264/0.49	0.70/0.87	
Coverage, *R*$_{int}$	0.98, 0.036	0.98, 0.099	1, 0.051	1, 0.0429	
***F*000**	500	497	500	501	495
Parameters refined	43	40	43	43	70
***R, wR* (obs)**	0.0248, 0.0745	0.0623, 0.1169	0.0121, 0.0303	0.0142, 0.036	
***R, wR* (all)**	0.0271, 0.0762	0.1051, 0.1306	0.0128, 0.0311	0.0152, 0.0372	
***GOF* (obs, all)**	1.49, 1.51	1.61, 1.75	1.41, 1.43	1.36, 1.37	1.88
Weighing scheme	$1/(\sigma^2(I)+0.0016I^2)$	$1/(\sigma^2(I)+0.0009I^2)$	$1/(\sigma^2(I)+0.0004I^2)$	$1/(\sigma^2(I)+0.0004I^2)$	
$\Delta\rho_{min}/\Delta\rho_{max}$ (e$^-$/Å^3)	−0.44/0.82	−2.28/3.21	−0.17/0.15	−0.22/0.22	−3.25/1.73
Ca1; 2/3,1/3,*z*					
z	0.00138(10)	0.0014(4)	0.00174(5)	0.00144(5)	0.0003(4)
***U*$_{eq}$**	0.0120(2)	0.0095(7)	0.01358(15)	0.01295(16)	0.0474(8)
***u*$_{11}$**	0.0140(3)	0.0108(8)	0.01357(18)	0.0156(2)	
***u*$_{22}$**	0.0140(3)	0.0108(8)	0.01357(18)	0.0156(2)	
***u*$_{33}$**	0.0080(4)	0.0067(14)	0.0136(3)	0.0077(3)	
***u*$_{12}$**	0.00702(15)	0.0054(4)	0.00678(9)	0.00778(10)	
Ca2; *x*,*y*,1/4					
x	0.99363(7)	0.9940(2)	0.99410(4)	0.99380(4)	0.9907(2)
y	0.24522(7)	0.2459(2)	0.24700(4)	0.24534(4)	0.2481(2)
***U*$_{eq}$**	0.0119(2)	0.0095(8)	0.01399(16)	0.01242(18)	0.0383(5)
***u*$_{11}$**	0.0155(4)	0.0119(10)	0.00946(18)	0.0094(2)	
***u*$_{22}$**	0.0180(4)	0.0128(11)	0.0184(2)	0.0186(2)	
***u*$_{33}$**	0.0074(4)	0.0072(11)	0.0098(2)	0.0075(3)	
***u*$_{12}$**	0.0123(3)	0.0088(9)	0.00372(13)	0.00565(16)	
P; *x*,*y*,1/4					
x	0.36971(9)	0.3694(3)	0.37004(5)	0.36978(5)	0.3689(3)
y	0.39970(9)	0.3994(3)	0.40038(5)	0.39967(5)	0.3992(3)
***U*$_{eq}$**	0.0061(2)	0.0042(11)	0.0073(2)	0.0093(2)	0.0318(8)
Occ, m.a.n.	14.34(8)	14.5(2)	14.44(6)	14.90(5)	13.49(10)
***u*$_{11}$**	0.0080(4)	0.0039(14)	0.0078(3)	0.0100(2)	
***u*$_{22}$**	0.0067(4)	0.0047(13)	0.0086(2)	0.0102(3)	
***u*$_{33}$**	0.0051(4)	0.0050(15)	0.0071(3)	0.0091(3)	
***u*$_{12}$**	0.0047(3)	0.0029(10)	0.00518(16)	0.00611(17)	
O1; *x*,*y*,1/4					
x	0.4858(3)	0.4854(8)	0.48610(13)	0.48571(16)	0.4869(5)
y	0.3299(3)	0.3297(7)	0.33149(15)	0.33008(18)	0.3381(5)
***U*$_{eq}$**	0.0139(6)	0.011(3)	0.0152(5)	0.0145(5)	0.0324(15)
***u*$_{11}$**	0.0184(11)	0.010(3)	0.0197(6)	0.0145(7)	
***u*$_{22}$**	0.0137(10)	0.012(3)	0.0118(5)	0.0213(7)	
***u*$_{33}$**	0.0148(10)	0.017(4)	0.0170(6)	0.0119(6)	
***u*$_{12}$**	0.0119(9)	0.009(3)	0.0100(5)	0.0120(5)	
O2; *x*,*y*,1/4					
x	0.4655(3)	0.4654(8)	0.46567(14)	0.46479(15)	0.4676(6)
y	0.5877(3)	0.5869(7)	0.58842(14)	0.58684(16)	0.5899(6)

Table S2 (continued): Crystal **s**tructure data refined from single-crystal X-ray diffraction data of core and fibrous apatite and powder X-ray diffraction of core apatite (last column).

	Core apatite	**Fibrous apatite**	**Core apatite**	**Fibrous apatite**	**Core apatite**
U_{eq}	0.0165(6)	0.014(3)	0.0200(4)	0.0179(5)	0.032(2)
u_{11}	0.0110(11)	0.015(4)	0.0134(5)	0.0182(6)	
u_{22}	0.0139(10)	0.003(3)	0.0185(5)	0.0118(6)	
u_{33}	0.0243(11)	0.024(5)	0.0280(6)	0.0263(6)	
u_{12}	0.0061(9)	0.004(3)	0.0077(5)	0.0096(6)	
O3; x,y,z					
x	0.25853(18)	0.2590(6)	0.25898(9)	0.25831(10)	0.2561(4)
y	0.3437(2)	0.3432(6)	0.34449(12)	0.34325(13)	0.3354(5)
z	0.0702(2)	0.0699(7)	0.06974(17)	0.06990(13)	0.0816(5)
U_{eq}	0.0206(5)	0.015(2)	0.0233(4)	0.0202(5)	0.0433(11)
u_{11}	0.0354(10)	0.013(2)	0.0379(5)	0.0193(5)	
u_{22}	0.0178(8)	0.026(3)	0.0176(4)	0.0365(6)	
u_{33}	0.0151(8)	0.008(3)	0.0218(7)	0.0110(6)	
u_{12}	0.0181(7)	0.012(2)	0.0196(4)	0.0187(5)	
u_{13}	−0.0094(7)	−0.004(2)	−0.0112(4)	−0.0041(3)	
u_{23}	−0.0057(6)	−0.010(2)	−0.0065(4)	−0.0074(4)	
X1, 0,0,1/4					
U_{iso}	0.013(2)	0.042(6)	0.0149(11)	0.0220(12)	0.076(5)
Occ, m.a.n.	5.94(18)	8.8(7)	6.25(9)	7.30(12)	8.3(3)
X2, 0,0,z					
z	0.343(2)		0.3833(14)	0.3522(12)	0.395(15)
U_{iso}	0.036(4)		0.0079(15)	0.017(3)	0.066(4)
Occ, m.a.n.	2.40(14)		2.41(6)	1.27(7)	1.24(14)

Both single-crystal and powder X-ray diffraction data were refined in space group $P6_3/m$ (No. 176). Single-crystal data were fitted by full matrix least-squares in Jana2006 on F^2. Powder diffraction data were refined in DIFFRAC.TOPAS using pseudo-Voigt profile shape function. Background-corrected agreement factors (in %) are as follows R_{Bragg} =3.781; R_{exp}= 4.44; R_{wp}= 8.37; R_p= 5.81; GOF= 1.88; DW= 0.66.

Table S3: Chemical compositions and recalculated empirical formulae of epidote-group minerals, actinolite-asbestos and amphibole relicts, chlorite and micas.

	allanite-(Ce)		epidote			actinolite-asbestos		edenite			chamosite		clinochlore			annite		ferrian-phlogopite		phlogopite	
	n = 23	σ	n = 17	σ		n = 23	σ	n = 18	σ		n = 14	σ	n = 6	σ		n = 17	σ	n = 8	σ	n = 6	σ
SiO_2	31.39	1.14	36.70	1.19	SiO_2	53.76	1.40	50.54	1.01	SiO_2	32.44	3.58	33.73	2.36	SiO_2	36.49	0.43	39.21	1.07	42.83	0.55
TiO_2	n.a.	n.d.	n.a.	n.d.	TiO_2	0.11	0.07	0.54	0.15	TiO_2	0.04	0.02	0.06	0.02	TiO_2	0.32	0.19	0.80	0.18	1.33	0.19
Al_2O_3	17.42	2.28	21.89	2.65	Al_2O_3	1.45	0.84	4.04	0.42	Al_2O_3	15.83	2.05	15.84	1.95	Al_2O_3	10.41	0.35	10.64	0.32	10.51	0.29
Cr_2O_3	b.d.l.	n.d.	b.d.l	n.d.	Cr_2O_3	n.a.	n.d.	n.a.	n.d.	Cr_2O_3	n.a.	n.d	n.a.	n.d.	Cr_2O_3	n.a.	n.d.	n.a.	n.d.	n.a.	n.d.
V_2O_3	0.56	0.90	0.20	0.09	V_2O_3	n.a.	n.d.	n.a.	n.d.	V_2O_3	n.a.	n.d.	n.a.	n.d.	V_2O_3	n.a.	n.d.	n.a.	n.d.	n.a.	n.d.
Y_2O_3	0.26	0.10	0.34	0.20	Y_2O_3	n.a.	n.d.	n.a.	n.d.	Y_2O_3	n.a.	n.d.	n.a.	n.d.	Y_2O_3	n.a.	n.d.	n.a.	n.d.	n.a.	n.d.
La_2O_3	5.97	1.30	0.90	0.65	La_2O_3	n.a.	n.d.	n.a.	n.d.	La_2O_3	n.a.	n.d.	n.a.	n.d.	La_2O_3	n.a.	n.d.	n.a.	n.d.	n.a.	n.d.
Ce_2O_3	12.84	1.76	2.24	2.03	Ce_2O_3	n.a.	n.d.	n.a.	n.d.	Ce_2O_3	n.a.	n.d.	n.a.	n.d.	Ce_2O_3	n.a.	n.d.	n.a.	n.d.	n.a.	n.d.
Pr_2O_3	1.65	0.29	0.82	0.20	Pr_2O_3	n.a.	n.d.	n.a.	n.d.	Pr_2O_3	n.a.	n.d.	n.a.	n.d.	Pr_2O_3	n.a.	n.d.	n.a.	n.d.	n.a.	n.d.
Nd_2O_3	2.88	0.42	1.08	0.88	Nd_2O_3	n.a.	n.d.	n.a.	n.d.	Nd_2O_3	n.a.	n.d.	n.a.	n.d.	Nd_2O_3	n.a.	n.d.	n.a.	n.d.	n.a.	n.d.
Fe_2O_3	3.49	1.94	9.61	1.79	Fe_2O_3	0.06	0.07	2.12	0.65	Fe_2O_3	n.c.	n.d.	n.c.	n.d.	Fe_2O_3	n.c	n.d.	n.c	n.d.	n.c	n.d.
FeO	10.13	1.11	3.78	2.06	FeO	15.98	2.97	10.88	3.16	FeO	26.97	3.24	21.34	2.34	FeO	33.04	1.61	25.07	1.51	10.98	1.03
MnO	0.161	0.10	0.14	0.08	MnO	0.21	0.09	0.13	0.12	MnO	0.23	0.09	0.24	0.07	MnO	0.13	n.d.	0.12	0.02	0.09	n.d.
MgO	0.29	0.16	0.45	n.d.	MgO	14.55	2.57	16.27	2.38	MgO	10.71	1.86	13.95	0.99	MgO	5.86	1.06	10.52	0.95	20.40	0.61
CaO	11.97	1.22	21.14	2.29	CaO	10.56	1.84	10.37	0.44	CaO	0.79	0.56	0.99	0.51	CaO	0.07	0.04	0.21	0.10	0.08	0.03
SrO	b.d.l.	n.d.	0.08	0.04	SrO	n.a.	n.d.			SrO	n.a.	n.d.	n.a.	n.d.	SrO	n.a.	n.d.	n.a.	n.d.	n.a.	n.d.
Na_2O	n.a.	n.d.	n.a.	n.d.	Na_2O	0.22	0.10	2.84	0.57	Na_2O	0.07	0.03	0.05	0.01	Na_2O	0.12	0.02	0.11	0.03	0.39	0.08
K_2O	n.a.	n.d.	n.a.	n.d.	K_2O	0.13	0.06	0.40	0.17	K_2O	0.92	0.67	0.35	0.40	K_2O	8.49	0.13	7.93	0.42	8.60	0.40
F	b.d.l	n.d.	b.d.l	n.d.	F	b.d.l.	n.d.	1.71	0.44	F	b.d.l.	n.d.	b.d.l.	n.d.	F	b.d.l.	n.d.	b.d.l.	n.d.	4.42	0.09
Cl	n.a.	n.d.	n.a.	n.d.	Cl	0.22	0.15	0.12	0.03	Cl	0.06	n.d.	n.d.	n.d.	Cl	4.88	0.39	2.91	0.44	0.23	0.07
H_2O (calc)	n.d.	n.d.	n.d.	n.d.	H_2O (calc)	2.00	0.07	1.23	0.18	H_2O (calc)	11.30	0.26	11.63	0.32	H_2O calc	0.64	0.12	1.23	0.13	1.94	0.02
O=F, Cl	n.d.	n.d.	n.d.	n.d.	O=F, Cl	0.05	0.03	0.75	0.18	O=F, Cl	n.d.	n.d.	n.d.	n.d.	O=F,Cl	1.10	0.09	0.66	0.10	1.91	0.05
Total	98.71	1.55	98.15	0.74	Total	100.34	0.74	100.43	0.90	total	87.30	2.11	86.52	2.35	Total	99.20	0.75	98.05	0.68	99.82	0.97
Si	3.007	0.035	3.003	0.013	Si	7.798	0.111	7.322	0.093	Si	3.385	0.356	3.481	0.228	Si	3.000	0.017	3.068	0.051	3.103	0.028
Al(IV)	0.037	n.d.	n.d.	n.d.	Al(IV)	0.184	0.108	0.667	0.092	Al(IV)	0.615	0.356	0.519	0.228	Al(IV)	0.996	0.017	0.928	0.046	0.890	0.023
T	3.000		3.000		T	8.000				T	4.000		4.000		Ti	0.020	0.012	0.047	0.010	0.073	0.010
Ti					Ti	0.013	0.008	0.047	0.021	Ti	0.004	0.001	0.004	0.001	Fe^{3+}(T)	0.013	0.005	0.030	n.d.	0.015	n.d.
Al(VI)	1.839	0.187	2.016	0.205	Al(VI)	0.075	0.050	0.045	0.047	Al(VI)	1.365	0.123	1.404	0.149	T						
V	0.045	0.070	0.011	0.007	Fe^{3+}(M)	0.106	0.078	0.231	0.072	Fe^{2+}	2.397	0.306	1.842	0.206	Al(VI)	0.018	0.022	0.061	0.039	0.016	n.d.
Fe^{3+}(M)	0.242	0.146	0.538	0.145	Fe^{2+}	1.682	0.457	1.191	0.436	Mn	0.020	0.008	0.021	0.007	Fe^{3+}(M)	0.010	0.035	0.093	0.059	0.062	0.026
Fe^{2+}	0.759	0.090	0.265	0.151	Mg	3.138	0.507	3.507	0.483	Mg	1.691	0.276	2.146	0.155	Fe^{2+}	2.196	0.118	1.546	0.119	0.597	0.079
Mn	0.012	0.009	0.010	0.007	C	5.000		5.000		tot M	5.475	0.333	5.417	0.212	Mn	0.009	0.002	0.008	0.001	0.006	n.d.
Mg	0.040	0.022	0.012	0.030	Mn	0.029	0.08	0.021	0.010	M vacancy	0.525	0.333	0.583	0.212	Mg	0.717	0.123	1.227	0.098	2.203	0.058
M	2.937		2.852		Fe^{2+}	0.263	0.261	0.141	0.076	Ca	0.090	0.062	0.111	0.058	M						
Y	0.013	0.005	0.015	0.009	Ca	1.674	0.273	1.613	0.078	Na	0.015	0.006	0.010	0.002	Ca	0.006	0.003	0.018	0.008	0.007	0.003
La	0.202	0.046	0.021	0.024	Na	0.037	0.001	0.239	0.077	K	0.124	0.091	0.046	0.052	Na	0.019	0.003	0.016	0.005	0.055	0.011
Ce	0.429	0.064	0.074	0.070	B	2.000		2.000		tot	0.206	0.153	0.163	0.098	K	0.891	0.012	0.792	0.045	0.794	0.034
Pr	0.055	0.009	0.011	0.013	Na	0.024	0.015	0.484	0.189	OH	7.998	0.005	8.000	0.000	A						
Nd	0.094	0.013	0.034	0.027	K	0.025	0.011	0.073	0.032	F	n.d.	n.d.	n.d.	n.d.	OH	1.320	0.059	1.613	0.063	0.959	0.028
Ca	1.166	0.090	1.742	0.160	A	0.049	0.024	0.558	0.177	Cl	0.011	n.d.	n.c.	n.d.	F	n.d.	n.d.	n.d.	n.d.	1.014	0.022
Sr	n.d.	n.d.	0.002	0.002	OH	1.946	0.038	1.189	0.196	tot A	8.000		8.000		Cl	0.680	0.059	0.387	0.063	0.028	0.008
A	1.999		1.899		F	n.d.	n.d.	0.829	0.060												
∑ + charges	24.740	0.337	24.215	0.362	Cl	0.054	0.038	0.029	0.007												
∑ - charges	25.027	0.007	25.007	0.005	W	2.000		2.000													
					SUM T,C,B,A	15.049	0.024	15.558	0.177												

Explanatory notes: n.a – not analyzed; n.c. – not calculated; n.d – not determined; b.d.l. – below detectrion limit

Table S4: Chemical compositions and recalculated empirical formulae of plagioclase, titanite, ilmenite and magnetite.

plagioclase						
	n=14	σ	14.	25.	26.	28.
SiO_2	65.55	0.95	55.45	50.81	49.79	47.69
TiO_2	0.03	n.d.	0.06	b.d.l.	b.d.l.	0.03
Al_2O_3	21.35	0.61	27.78	30.2	30.96	32.18
Cr_2O_3	n.a.	n.d.	n.a.	n.a.	n.a.	n.a.
V_2O_3	n.a.	n.d.	n.a.	n.a.	n.a.	n.a.
Fe_2O_3	0.31	0.24	1.17	0.76	0.17	0.57
FeO	0.11	0.17	0.00	0.00	0.57	0.00
MnO	b.d.l.	n.d.	b.d.l.	b.d.l.	b.d.l.	b.d.l.
MgO	b.d.l.	n.d.	b.d.l.	b.d.l.	b.d.l.	b.d.l.
CaO	2.49	0.70	10.92	14.39	14.96	16.71
SrO	n.a.	n.d.	n.a.	n.a.	n.a.	n.a.
Na_2O	10.26	0.37	5.51	3.48	2.95	2.11
K_2O	0.21	0.21	0.18	0.09	0.09	0.05
F	n.a.	n.d.	n.a.	n.a.	n.a.	n.a.
Cl	n.a.	n.d.	n.a.	n.a.	n.a.	n.a.
H_2O calc	n.c.	n.d.	n.c.	n.c.	n.c.	n.c.
O=F,Cl	n.c.	n.d.	n.c.	n.c.	n.c.	n.c.
Total	100.31	0.52	101.07	99.73	99.49	99.34
Si	2.878	0.033	2.481	2.325	2.289	2.205
Ti	0.001	n.d.	0.002	b.d.l.	b.d.l.	0.001
Al	1.105	0.033	1.465	1.629	1.678	1.754
Fe^{3+}	0.011	0.008	0.041	0.027	0.006	0.02
Fe^{2+}	0.004	0.006	0.000	0.000	0.022	0.000
Mn	b.d.l.	n.d.	b.d.l.	b.d.l.	b.d.l.	b.d.l.
Mg	b.d.l.	n.d.	b.d.l.	b.d.l.	b.d.l.	b.d.l.
Ca	0.117	0.033	0.523	0.705	0.737	0.828
Na	0.873	0.030	0.478	0.309	0.263	0.189
K	0.012	0.012	0.010	0.005	0.005	0.003
tot. cat.	5.000		5.000	5.000	5.000	5.000
tot. oxy.	7.994	0.006	7.991	7.996	7.997	7.997
$Si+Ti+Al+Fe^{3+}$	3.994	0.006	3.986	3.981	3.973	3.979
ideal	4.000		4.000	4.000	4.000	4.000
Ca+Na+K	1.002	0.006	1.012	1.019	1.005	1.020
ideal	1.000		1.000	1.000	1.000	1.000

titanite		
	n=13	σ
SiO_2	31.02	0.30
TiO_2	33.48	1.72
Al_2O_3	4.49	1.07
Cr_2O_3	b.d.l.	n.d.
V_2O_3	0.24	0.05
Fe_2O_3	1.47	0.68
FeO	n.c.	n.d.
MnO	b.d.l.	n.d.
MgO	b.d.l.	n.d.
CaO	29.08	0.51
SrO	n.a.	n.d.
Na_2O	b.d.l.	n.d.
K_2O	b.d.l.	n.d.
F	0.55	0.12
Cl	n.a.	n.d.
H_2O calc	n.c.	n.d.
O=F	0.23	0.05
Total	99.90	0.55
Si	1.037	0.008
Ti	0.800	0.042
Al	0.168	0.040
V	0.006	0.001
Fe	0.035	0.009
Ca	0.989	0.016
F	0.055	0.011
O	4.948	0.186

ilmenite		
	n=22	σ
SiO_2	b.d.l.	n.d.
TiO_2	49.80	0.82
Al_2O_3	0.04	0.005
Cr_2O_3	0.09	n.d.
V_2O_3	0.63	0.13
Fe_2O_3	n.c.	n.d.
FeO	47.17	0.97
MnO	1.14	0.36
MgO	0.52	0.22
CaO	0.06	0.03
SrO	n.a.	n.d.
Na_2O	b.d.l.	n.d.
K_2O	b.d.l.	n.d.
F	b.d.l.	n.d.
Cl	n.a.	n.d.
H_2O calc	n.c.	n.d.
O=F	n.c.	n.d.
Total	99.31	0.51
Ti	0.961	0.013
Al	0.001	0.0002
Cr	0.002	n.d.
V	0.013	0.003
Fe	1.012	0.023
Mn	0.025	0.008
Mg	0.020	0.008
Ca	0.002	0.001

magnetite		
	n=11	σ
SiO_2	b.d.l.	n.d.
TiO_2	9.08	1.09
Al_2O_3	1.11	0.19
Cr_2O_3	0.53	0.11
V_2O_3	3.38	0.47
Fe_2O_3	45.09	1,61
FeO	38.69	1.10
MnO	0.35	0.08
MgO	0.13	0.07
CaO	0.06	0.02
SrO	n.a.	n.d.
Na_2O	b.d.l.	n.d.
K_2O	b.d.l.	n.d.
F	b.d.l.	n.d.
Cl	n.a.	n.d.
H_2O calc	n.c.	n.d.
O=F	n.c.	n.d.
Total	98.38	0.86
Ti	0.262	0.030
Al	0.050	0.009
Cr	0.016	0.003
V	0.104	0.014
Fe^{3+}	1.304	0.052
Fe^{2+}	1.244	0.028
Mn	0.011	0.003
Mg	0.007	0.004
Ca	0.003	0.001
∑ cation	3.000	n.d.

Explanatory notes: n.a — not analyzed; n.c. — not calculated; n.d — not determined; b.d.l. — below detectrion limit